Crustal Permeability Changes Inferred From Seismic Attenuation: Impacts on Multi-Mainshock Sequences

Luca Malagnini[1*], Tom Parsons[2], Irene Munafò[1], Simone Mancini[3], Margarita Segou[4], and Eric L. Geist[2]

[1]Istituto Nazionale di Geofisica e Vulcanologia, Sezione di Roma 1, Rome, Italy.

[2]United States Geological Survey, Moffett Field, CA, USA.

[3]Scuola Superiore Meridionale, Università degli Studi di Napoli Federico II, Naples, Italy.

[4]British Geological Survey, Edinburgh, UK

[*]Corresponding author: Luca Malagnini (luca.malagnini@ingv.it)

Key Points:

1) Seismic attenuation is fundamentally linked to crustal permeability
2) During a seismic sequence, bulk permeability of crustal rocks and pore-fluid pressure are modulated by cumulative seismic stress drop
3) The seismic sequence of the Central Apennines (2016-17) is a long episode of fluid diffusion

Abstract

Measuring variations of seismic attenuation over time, while requiring extreme measurement sensitivity, provides unique insights into the dynamic state of stress in the Earth's crust at depth. We analyze seismic data from earthquakes of the 2016-2017 Central Apennines seismic sequence and obtain high-resolution time histories of seismic attenuation in a wide frequency band (0.5-30 Hz) that are characterized by strong earthquake dilatation-induced fluctuations (deep), as well as damage-induced ones (shallow). The cumulative elastic stress drop after the sequence causes negative dilatation, reduced permeability and seismic attenuation. We observe that $\mathbf{M} \geq 3.5$ earthquake occurrence vs. time and distance is consistent with fluid diffusion, and that these diffusion signatures are associated with changes in seismic attenuation during the first days of the Amatrice, Visso-Norcia, and Capitignano sub-sequences. We conclude that coseismic permeability changes, partially evidenced by seismic attenuation, create fluid diffusion pathways that are at least partly responsible for triggering multi-mainshock seismic sequences.

Plain Language Summary

We investigate the Central Apennines (Italy) seismic sequence that started with the 24 August 2016 M5.97 Amatrice shock, and led to a cascade of 11 more M≥5 shocks, including the 30 October 2016 M6.33 Norcia mainshock. We measure changes in seismic attenuation vs. time, observe patterns of earthquake occurrence vs time and distance that are consistent with fluid diffusion, and calculate crustal the dilatation induced by the sequence. We support a model of permeability-driven seismic attenuation: under extensional tectonics, the elastic stress drop after the seismic sequence results in negative dilatation, reduced permeability, and reduced attenuation. During the first days following the main events of the sequence, fluid diffusion is associated with changes in seismic attenuation. What emerges is that: (i) coseismic negative dilatation following large normal fault earthquakes closes fluid-filled cracks, driving fluids out, (ii) coseismic damage to fault zones and in the shallow crust provides pathways for fluid transfer, (iii) seismic attenuation is temporarily decreased during this time, (iv) short-lived (<10 days) diffusion into adjacent fault zones and the shallow crust triggers subsequent earthquakes, (v) seismic attenuation gradually recovers after this redistribution of fluids, (vi) the process repeats until regional failure stress is exhausted.

1 Introduction

Until recently, seismic attenuation was considered constant in time; at least it was studied as such (e.g., Malagnini and Dreger, 2016). Previous work on temporally changing attenuation was performed in volcanic settings (Titzschkau et al., 2010), or after strong-motion events (e.g., Chen et al., 2015; Kelly et al., 2013). Then a study by Malagnini and colleagues (2019) demonstrated that total seismic attenuation fluctuates periodically, responding to slow-varying seasonal stresses and solid Earth tides. They also showed sharp increases of the attenuation parameter $Q_S^{-1}(f,t)$ due to shallow rock damage after strong-motion episodes, and either increases or decreases of $Q_S^{-1}(f,t)$ due to static stress transfer from earthquakes occurring on nearby faults.

Malagnini and Parsons (2020) interpreted the fluctuations of $Q_S^{-1}(f,t)$ in terms of changes in permeability driven by variable compressional stresses. Of particular interest was the variation of crustal attenuation related to strong-motion earthquakes. Malagnini and Parsons envisioned two competing effects in the aftermath of a mainshock: (1) shallow damage that mostly affected relatively low-frequency surface waves (0.5-1.5 Hz, where 0.5 Hz was the minimum frequency observed), and (2) stress-induced dilatation from the static stress drop of the mainshocks of the sequence (either from each individual earthquake, or cumulatively).

Seismic attenuation has two fundamental components: (1) redistribution of seismic radiation in time and space by scattering behind the wavefront of interest (either direct P or S, e.g., Hoshiba 1995; Akinci et al., 2020); and (2) anelasticity, which transforms the elastic energy carried by stress waves into heat. This study deals with the anelastic dissipation of seismic energy. Dissipated seismic energy (converted into heat) has two contributions: (1) energy dissipated in the immediate vicinity of the fault, especially at high frequency, and (2) elastic energy dissipated along the path traveled between the surface of the volume that encapsulates the source (see previous point) and the receiver. By definition, dissipation of the first kind cannot be observed, and is inevitably included in a more general budget named “*breakdown work*” (Tinti et al., 2005) that contains frictional heat generated by fault slip, or slip-rate, weakening phase, and energy spent on changing surfaces, including new fault surface, the surface obtained by the formation of new fragments and the comminution of existing ones, all the way to the formation of fault gouge.

Another distinction can be made between two different contributions to attenuation of elastic energy of traveling stress waves that are of roughly equivalent importance (Hanks, 1982; Kilb et al., 2012), occurring either along the crustal path, or in the immediate vicinity of the free surface (assuming a surface recording device). Our study deals only with dissipation occurring along crustal propagation. Lastly, for the sake of completeness, we remind the reader that in very shallow, fluid-rich environments, bubble production induced by traveling stress-waves may also cause significant attenuation (Tisato et al., 2015).

Crustal fluids are thought to play a primary role in anelastic attenuation along crustal paths. The physical phenomenon is that of viscous dissipation of seismic energy into heat within interstitial fluids. In fact, it is believed (e.g., O'Connell and Budiansky, 1977) that the elastic energy carried by stress waves is dissipated through two mechanisms: viscous damping acting on the pore fluids that are forced to move within isolated cracks, and stress-induced fluid flow between interconnected cracks. The dimensions of rock-permeating cracks, the characteristics of their statistical distribution, and the degree of their interconnection (i.e., the permeability of crustal rocks), completely define the frequency dependence of the anelastic attenuation parameter Q_i^{-1}, where "*i*" can be either P or S (without loss of generality we can limit our case to direct S-waves).

Depending on the frequency of oscillation, the interconnection of cracks within the network and the level of saturation, pore fluids oscillate within and between cracks in saturated or partially saturated rocks at low frequencies. A drained regime is attained when the period of oscillation is large enough (in units of fluid relaxation time) to allow inter-crack flow. Alternatively, they can oscillate within the same crack at intermediate frequencies in either saturated or partially saturated rocks. An isolated regime is attained when there is not enough time (in units of fluid relaxation time) to oscillate between cracks, although there is enough time for intra-crack oscillations. A *glued* regime occurs when the period of oscillation is shorter than the relaxation time of the viscous fluid within the crack, and the fluid causes negligible dissipation (O'Connell and Budiansky, 1977). Transitions between different regimes can be observed by sweeping through a wide frequency band, where peaks in the attenuation parameter $\left(Q^{-1}(f)\right)$ are expected to correspond to each regime transition (O'Connell and Budiansky, 1977). Dry conditions may also occur in specific natural environments (e.g., the Moon, see Mitchell, 1995), with no viscous dissipation.

If crack density and connectivity directly determine the permeability of crustal rocks, the average crack orientation determines its anisotropic behavior, and its sensitivity to static stress changes, like the stress transfer from a seismic dislocation occurring on a nearby fault. An interesting example of this effect is exhibited after induced unclamping of the San Andreas Fault (SAF) by the **M**6.5 San Simeon earthquake (Johanson and Bürgmann, 2010; Malagnini et al., 2019). In addition to static stress variations, weak motions excited by large distant earthquakes (at regional to teleseismic distances) can influence the permeability of crustal rocks if they radiate enough energy at relatively low-frequency (~0.05 Hz, see Roeloffs, 1998). The proposed mechanism is that of breaking and subsequently flushing away colloidal deposits that clog rock pores and cracks, resulting in large increases in rock permeability, stream discharge, (Roeloffs, 1998; Manga et al., 2016; Manga and Brodsky, 2006; Brodsky et al., 2003), and increased seismic attenuation (Malagnini et al., 2019). The same mechanism may be responsible for triggering distant earthquakes by teleseismic waves through fluid diffusion caused by increased permeability (Parsons et al., 2017). Finally, the results of a numerical experiment performed by Barbosa et al. (2019) show that seismically induced viscous shearing within cracks of the order of those initiating unclogging (0.1 to 1 Pa) are plausible for strain magnitudes and frequencies typically observed in field and laboratory measurements.

The colloidal particles mobilized in a specific crustal volume by the fluid flow-induced shear stresses during some weak shaking may re-aggregate in adjacent rock volumes, especially if the latter are bounded by an impermeable surface (like the case of the SAF at Parkfield, as documented by Malagnini and Parsons, 2020), decreasing rock permeability and the attenuation parameter. The described effect has been observed in lab experiments by Liu and Manga (2009), who stated that lab experiments confirm that dynamic stresses and time-varying flow can change permeability, and both permeability increases and decreases may be possible.

Another physical mechanism responsible for the increased rock permeability (and seismic attenuation) indirectly observed after shaking is that of strong motion-induced rock damage (Kelly et al., 2013; Rubinstein and Beroza, 2005; Malagnini and Parsons, 2020). As shown along the SAF at Parkfield by Kelly et al. (2013) and Malagnini et al. (2019), rock damage heals over several years, most probably by the precipitation of minerals and colloidal particles into the crack network, and the consequent reduction of permeability.

In this paper we measure anelastic attenuation based on peak amplitude ratios calculated at two different hypocentral distances. Peak amplitudes are from weak- and strong-motion, narrowband-filtered time histories. Interpolations at specific hypocentral distances are calculated through simple regressions, made possible by a mathematical tool called Random Vibration Theory (Cartwright and Longuet-Higgins, 1956, see later). The latter, together with the Parseval equality, allows the use of the Convolution Theorem on peak amplitudes.

We suggest that the long-term variation of the attenuation parameter after one or more main shocks is caused by permanent crustal dilatation (increased or decreased compressional stress caused by the cumulative effect of the main earthquakes' static stress drops). In regions subjected to extensional tectonics, like the one struck by the 2016-2017 seismic sequence of Amatrice-Visso-Norcia (Central Apennines, Italy), the cumulative stress drop causes a permanent reduction of the attenuation parameter, and thus of the permeability within the crustal volume affected by the seismicity, confirming the conceptual model by Muir-Wood and King (1993).

Our working hypothesis is that crustal anelastic attenuation is closely related to the characteristics of the crack population that permeates crustal rocks. Whereas the crack-fluid interaction under the excitation of traveling stress waves represents a difficult problem to be solved quantitatively, either numerically or analytically, it may be easier to propose meaningful physical interpretations about the nature of the variation of the empirical observation of attenuation changes over time. We note variations of $Q_S^{-1}(f,t)$ after the normal faulting earthquakes of the Central Apennines that show sharp drops after each main shock. Moreover, the cumulative effect of an entire seismic sequence is such that there is a notable and stable decrease of $Q_S^{-1}(f,t)$.

2 Data

The 2016-2017 Amatrice-Visso-Norcia (AVN) seismic sequence of the Central Apennines (Italy)

On 24 August 2016, at 01:36 UTC, an **M**5.97 earthquake struck the town of Amatrice. The main shock started a long seismic sequence characterized by two more main events (**M**5.87 Visso, on 26 October 2016, at 19:18 UTC, and the **M**6.33 Norcia, on 30 October 2016, at 06:40 UTC; Figure 1A). The seismic sequence affected a large region (see the seismicity distribution shown in Figure 1B), and lasted until the end of January 2017. On January 18, 2017, a sequence of smaller shocks (**M**5.43 was the largest shock) marched through the deep part of the Campotosto fault, with epicenter near Capitignano (e.g., Cheloni et al., 2019; Falcucci et., 2018; Gori et al., 2019), with four events with **M**>5 (Figure 1A). After the Capitignano subsequence, the seismic activity of the region faded away and returned to the background level by late 2017. A rough display of the spatio-temporal evolution of the seismic sequence is provided in Figure S1.

The AVN seismic sequence contained the largest earthquake ever recorded in the Central Apennines. The sequence was recorded by a dense modern network of seismometers and accelerometers, and the collected data set provides a unique opportunity to study earthquake-related phenomena in the region. Together with the one collected during the 2009 L'Aquila seismic sequence, the AVN data set allows us to study earthquake sources and wave propagation phenomena with unprecedented accuracy for this region.

The final data set used for attenuation calculations consisted of 3,236 earthquakes recorded by 67 weak-motion 3-component stations belonging to Rete Sismica Nazionale (RSN), run by Istituto

Nazionale di Geofisica e Vulcanologia (INGV, Figure 1B, see Catalog provided as a Supporting Information). Events were gathered in the period between 07/01/2013 and 31/08/2020 with 2.0<**M**<6.33. The data set also included 83 events recorded by the Rete Accelerometrica Nazionale (RAN) for a total of 9,905 strong-motion waveforms. Station list is provided as Supporting Information. This study is based on a total of 200,132 individual-component waveforms. The histograms in Figure 2 describe the distributions of the magnitudes (M_L) of the events in our data set, hypocentral depths, and hypocentral distances of the recorded seismograms.

We only used seismograms with one individual event, no glitches, no holes, and no spurious noise. Seismograms with multiple (overlapping) events were either cut in the time window containing the specific event only, or removed from the data set. A total of 200,132 seismograms were chosen from 3,236 earthquakes with 2≤M≤6.0 occurring between January 7 2013 and August 20 2020 by visually inspecting a multitude of individual time histories by either Irene Munafò or Luca Malagnini. A signal-to-noise (S/N) ratio analysis was performed on the spectral content of each individual seismogram, as described by Malagnini et al. (2000). Also, during the sequence the magnitudes of the events in the data set are higher (and so is the S/N ratio). Finally, we used Random Vibration Theory in order to maximize the S/N ratio (we use peak values, not spectral amplitudes, see Malagnini and Dreger, 2016 for details). No noise issues can affect the variability of attenuation at low frequencies.

3 Methods

The technique used here evolved from the work by Raoof et al. (1999) and Malagnini et al. (2000), and is described by Malagnini et al. (2019) and Malagnini and Parsons (2020). The approach is based on a tool called Random Vibration Theory (RVT), developed by Cartwright and Longuet-Higgins (1956) for the analysis of tides, and subsequently widely used in ground motion analyses (e.g. Boore and Joyner, 1984). RVT allows the use of peak values of narrowband-filtered time histories in place of their Fourier amplitudes. Moreover, it allows using the Convolution Theorem for peak value analysis (for a detailed explanation, see Appendix A in Malagnini and Dreger, 2016). Exchanging Fourier amplitudes for peak values brings a huge improvement of the signal-to-noise ratios of the data used in the regressions, which is key in studying the fluctuations of the attenuation parameter.

The disadvantage of using RVT is that we lose the information on the peak arrival time, because in theory the peak can occur anywhere in the time history. We worked around this drawback in two ways: (1) we prescribed that the analysis be performed in the time window marked by the S-wave arrival and a minimum group velocity (1.5 km/s; (2) we visually inspected all the seismograms of the data set. This required us to visually inspect about 300,000 seismograms to generate a data set of 200,000+ good waveforms without multiple events in a time history, glitches, spurious peaks, data gaps, etc.. We gathered progressive groups of 40 consecutive earthquakes from our catalog of 3,236 earthquakes by moving forward one earthquake at a time as P=M-C+1, yielding overlapping subsets of C ordered consecutive events (C=40 in our case). Malagnini et al. (2019), tried subsets of 80-60-50-40-30 events, and explored the tradeoff between relatively more stable results obtained using a larger number of waveforms, and the loss of time resolution that comes with a larger number of earthquakes. They showed that no significant quality increment could be obtained (in terms of stability) with more than 40 events, but below that number the attenuation results were unstable. The issue of stability of the results vs. their time resolution is not important during a seismic sequence, when events are frequent, large, and each of them is recorded by many stations. The issue becomes more important during "regular" times, when earthquakes are infrequent, small, and do not have many recordings.

For each subset of 40 earthquakes we repeat the following steps: i) filter the N seismograms of the subset around a set of K central frequencies, $\{f_{c_\kappa}\}_{\kappa=1,\dots,K}$; ii) extract the peak amplitudes (A_n) at all individual frequencies and arrange them in a matrix form (one independent matrix for each central frequency, one line for each filtered seismogram, with no cross-frequency smoothing); iii) run the K regressions on all central frequencies using (1).

$$A_n(r_{ij}, t_j, f_{c_k}) = SRC_j(r_0, f_{c_k}) + D(r_{ij}, r_0, t_m, f_{c_k}) + SITE_i(f_{c_k}) + \epsilon_n, \quad (1)$$

In (1), $SRC_j(r_0, f_{c_k})$ refers to the contribution of the j^th^ source, normalized to a reference distance r_0, $SITE_i(f_{c_k})$ is the contribution of the i^th^ site, and $D(r_{ij}, r_0, t_m, f_{c_k})$ is a path term that accounts for the effect of crustal propagation. Note that path and source terms in (1) are normalized by a reference distance.

The parameter t_m represents the origin time of the m-*th* event of the current subset of ordered consecutive earthquakes, and for this study we chose $m = 1$; r_{ij} is the hypocentral distance between the *i-th* recording site and the *j-th* earthquake; r_0 is an arbitrary reference distance (we use $r_0 = 10$ km).

The *n-th* row of the matrix (1) refers to the *n-th* observation, the *j-th* column refers to the *j-th* seismic source, the *i-th* column refers to the *i-th* station, and *k=1,…,44* refers to the *k-th* regression (one regression per central frequency f_{c_k}). Finally, ϵ_n is the residual between the observation and the sum of the three terms describing the ground motion (we drop it in what follows).

$$A_n(r_{ij}, t_j, f_{c_k}) = log_{10}(PEAK[a_n(r_{ij}, t_j, f_{c_k})]), \quad (2)$$

Term $a_n(r_{ij}, t_j, f_{c_k})$ in (2) is the narrowband-filtered version of the n^th^ time history, relative to the i^th^ station, and to the j^th^ source. $PEAK[a_n(r_{ij}, t_j, f_{c_k})]$ in (2) indicates the peak value observed after the S-wave arrival and with a group velocity larger than 1.5 km/s; $t_j \neq t_m$ when $j \neq m$.

The inversion of (1) is performed after adding the following constraints:

$$D(r_{ij} = r_0, t_m, f_{c_k}) = 0, \quad (3)$$

$$\sum_{i=1}^{NSITE} [SITE_i(f_{c_k})]=0, \quad (4)$$

$$D_{l-1}(f_{c_k}) - 2D_l(f_{c_k}) + D_{l+1}(f_{c_k}) = 0, \tag{5}$$

∑ where: $l = 0,1, \ldots, L$, and L is the number of nodes defining a continuous piecewise-linear path term in a log-log space.

Constraints (3) effectively decouples the path term (representing total attenuation) from the combination of source and site terms. The reader should keep in mind that our working hypothesis is that the crust is laterally homogeneous in the studied region. Although this hypothesis is never completely true, it has worked reasonably well in many areas of the world (see studies by Malagnini and colleagues, including those on source scaling, e.g., Mayeda and Malagnini, 2009, Malagnini and Mayeda, 2010, Malagnini et al., 2008). Constraint (4) decouples the site and source terms and gives physical meaning to the latter (i.e., the source terms that would be recorded at the reference distance r_0 by the average network site, see Malagnini et al., 2000). Constraint (4) has no effect on our results, and we include it for completeness. Constraint (5) is a smoothing operation applied to the crustal propagation term, which minimizes the roughness of the solution and has negligible effects on our results.

For completeness, we note that the number of stations may not be strictly the same for each earthquake, adding some variability from earthquake to earthquake. Yet, they always contribute to the null average site term because the latter is not forced individually on each earthquake, but through the inversion of the matrix (1). This is done by adding an extra row of zeros in all columns, except for all columns corresponding to the horizontal site terms, where we insert a large number, comparable to the number of data points. An extra zero is added to the column of the observed amplitudes.

By inverting matrix (1), we obtain one set of source spectra, one set of site terms, and one smooth path term for each central frequency. Because of constraint (3), the path term is equivalent to an amplitude ratio between the attenuation at distances r_{ij} and r_0, that can be modeled for any distance r as:

$$D\left(r_1, r_0, t_m, f_{c_k}\right) = \left[\frac{g(r_1)}{g(r_0)} exp\left(-\frac{\pi f(r_1 - r_0)}{V_S Q_S(t_m, f_{c_k})}\right)\right], \tag{6}$$

where g(r) is a static attenuation function, piecewise-linear in log-log space, r_0 is an arbitrary hypocentral distance used for normalization (3), $Q_S^{-1}(t_m, f)$ is a measure of time-dependent attenuation at t=t_m, which is the focus of our research, $r_1 = 40$ km is a second arbitrary hypocentral distance, and V_S is shear-wave velocity. Crustal propagation is spatially sampled at a fixed set of hypocentral distances, in the 10 - 150 km range.

Figure 3a shows the total attenuation term $D\left(r_1, r_0, t_m, f_{c_k}\right)$ at a subset of sampling frequencies, with the indication of the durations of each one of the *m* time windows (each one contains 40 events) used to scan the entire period (horizontal black segments in Figure 3a). Moreover, Figure 3b is a 2-D representation of the fluctuations of the seismic attenuation parameter around its average value, $\Delta Q_S^{-1}(t_m, f)$, with the indications of the events of the sequences with **M**≥4.5 (epicenters in map of Figure 3c). The time-averaged attenuation parameter $\langle Q_S^{-1}(f)\rangle$ is shown in Figure 3d (averages calculated in two consecutive time windows: pre- and post-Amatrice. Note the reduction in the average attenuation parameter in the second time window. Note also that $\langle Q_S^{-1}(f)\rangle$ is described by a power law at high frequencies, but flattens just below 1 Hz, indicating that below 1 Hz frequencies, surface waves dominate between the two distances that are arbitrarily chosen to calculate the attenuation parameter. We can safely state that above 1 Hz all the peak values of the narrowband-filtered time histories are carried by direct S-waves. To reduce the error bars of the attenuation function, we apply a bootstrap procedure, in which 10% of the events of each time window are removed from the data set. 10 different regressions are run on the data set associated to t_m, and the 10 attenuation parameters $\left(Q_S^{-1}(t_m, f)|_i,\ i = 1, \ldots, 10\right)$ are averaged, obtaining smooth and reliable attenuation surfaces like those shown in Figure 4. A zoom on the most energetic part of the seismic sequence, between the Amatrice mainshock (08/24/2016) and 12/31/2016 is shown in Figure S3.

By calculating the average attenuation over time, removing the geometric attenuation calculated by Malagnini et al. (2011, their eq. (3)) for the adjacent region that was struck by the April 6 2009 L'Aquila earthquake, and subtracting it from eq. (6), we obtain anomalies of $Q_S^{-1}(t,f)$ that are plotted in Figure 4 (we drop the *m* subscript of the time variable from now on). The average is taken between 01/01/2013 (the beginning of our time window) and 23/08/2016 (the day before the Amatrice main shock) to enhance the effects of the seismic sequence. Finally, errors with respect to the average (d(log(1/Q)), calculated in the regressions for all time windows and for all frequencies, are shown in Figure S3.

Limitations of our approach

Scientific results must be thoroughly evaluated to understand hidden limitations of techniques. We point out the existence of issues of limited importance about the current application developed by Malagnini et al. (2019).

1. Trade-offs:

Tradeoffs are the inevitable drawback of any inverse problem. What we have available is equation (1), and the constraints that are forced onto the matrix. With such a limited set of tools, we are able to exploit our data set in many different ways, including the assessment of temporal variations of the site terms (Figure S4). Although some variability is inevitable, their collective behavior is totally acceptable for our purposes.

Yet, our results must be affected by unavoidable tradeoffs. As an example, if all sites simultaneously experienced the same amount of damage during some strong shaking, constraint (4) would force the changes in site attenuation that are common to all sites, through constraint (3), onto all source terms. Because shaking-related rock damage is a shallow consequence of earthquake-induced ground motion, we expect that an increase in site terms occurs at low frequency at the beginning of the sequence. Figure S4 documents such a change, which only affects a subset of recording stations and is counterbalanced by the rest of the sites.

Our working hypothesis may also look simple, but many studies demonstrated that it works in the Apennines, even in a region that is larger than the one struck by the 2016-2017 seismic sequence. The availability of seismometric data in the study area is enough to study the average behavior of the seismic attenuation, and its variability over time. Moreover, the sampled crustal volume (Figure 1) is large enough and well instrumented, so that a large number of stations sample the same crustal volume illuminated by the seismic events. This is especially true for the time window that includes the seismic sequence. In comparison, the time window between 01/01/2013 and 23/08/2016 shows a remarkably constant crustal attenuation pattern (except for the seasonal fluctuations, see Figures 3b and 4), in spite of the fact that in order to obtain enough events to have a decent time resolution we needed to select anything above M1.9 (i.e., scattered background seismicity).

Source and site terms are remarkably stable over the period between 01/01/2013 and 23/08/2016 (Figure S4), especially when compared to their behaviors during the sequence. It also appears that the more seismically active region of the Central/Northern Apennines between L'Aquila to Norcia, is (in relative terms) seismologically homogeneous, at least in terms of the velocity structure. For example, Herrmann et al. (2011) were successful in using the Central Italy Apennines (CIA) velocity model to reproduce broadband seismograms down to M2.8 - http://www.eas.slu.edu/eqc/eqc_mt/MECH.IT/). The broadband inversion of the moment tensors uses frequencies up to 0.15 Hz, that is, minimum wavelengths of 15-20 km.

We use a set of stations within 50 km of any of the mainshocks. Moreover, we always look at the same hypocentral distance of 40 km; earthquakes at larger distances can still contribute (mainly through the smoothing constraint (5)) to the value of D(r,f), yet they do so negligibly with respect to earthquakes at closer distance. We however looked at the same 1/Q plots at shorter and longer hypocentral distances (30 km and 80 km), obtaining virtually the same results (Figure S5 shows the variability of 1/Q at 80 km). Finally, regressions demonstrated to be extremely stable to random mislocations that are larger than the location precision (especially to outliers, see

Figure S6). The various arguments listed in the current subsection concur to establish confidence in our results.

2. Near-fault and off-fault effects:

The effect of seismic attenuation on observed amplitudes of ground motion refers to the integral of all the individual contributions experienced along the entire crustal path, from the immediate vicinity of the fault to the recording site. Because the effect is proportional to the duration that seismic waves are affected by some specific attenuation, we can write that:

$$\frac{T_{TOTAL}}{Q_{TOTAL}} = \frac{T_{NEAR-FAULT}}{Q_{NEAR-FAULT}} + \frac{T_{PATH}}{Q_{PATH}}. \tag{7}$$

As a consequence of (7), the fluctuations of Q in the fault zone could be larger than what we obtain. Note that the near-site contribution $\left(\frac{T_{SITE}}{Q_{SITE}}\right)$ is decoupled from that of the crustal propagation by constraint (3), and we do not need to take it into account. Also, the calculated value of $Q_S^{-1}(f,t)$ is an effective value that incorporates the effects of both processes of anelastic and scattering attenuation, and we do not attempt to discriminate between them. Lastly, we interpret the sharp increase in the seismic attenuation that occurs at low frequency after the onset of the Amatrice mainshock as the effect of rock damage at shallow depths, at or below 1.0 Hz in Figure 2 (lower frame) where surface waves dominate. Due to the nature of surface waves, we expect the effects of shaking-induced rock damage to extend down to less than a few hundred meters .

3. Causality:

We use overlapping subsets of 40 consecutive earthquakes, calculate the attenuation relative to each sub-set, and associate it to a specific time belonging to the time window spanned by the subset (in the current application, the time of occurrence of the first earthquake). Then the time window is shifted to the next earthquake available along the time axis, and a new subset of 40 earthquakes is obtained by including the 41st earthquake, and leaving out the first event. The second attenuation data point is calculated and associated to the occurrence time of the second earthquake of the entire data set. There will be times in which the time window spanned by 40 consecutive earthquakes is very long, about half a year before 24 August 2016, but as soon as the first main shock hits Amatrice, the interevent times get very small, down to a fraction of an hour (Figure 3a).

When the moving window hits the first mainshock, for 39 more time steps we include its effects (damage and dilatation reduction) on the resulting attenuation data points. We have a causality issue for whatever the choice of the occurrence time to associate with a specific data point (we chose the first origin time of the original ordered subset of 40 events, regardless of the actions of the bootstrap analysis. Malagnini et al., 2019 chose the median origin time, and another possible choice could be the average origin time, etc). We break the data set into two parts, before Amatrice, and from the Amatrice mainshock onward to avoid acausal effects. After the first mainshock, the sampling of the attenuation parameter is fine enough that we do not need to apply this procedure any more times (acausality is always present, but during the sequence, the time windows are very short, and we can neglect it for our purposes).

To aid in interpretation of attenuation observations, we add independent lines of investigation. We calculate coseismic dilatation to gain insight into where post-earthquake extension and compression occur and associated inferred crack opening or closing. We additionally conduct simple calculations of expected changes in relative fluid flow magnitudes and directions based on dilatation. We also examine the catalog for seismic patterns in time and space that are consistent with fluid diffusion signals.

We calculate the coseismic dilatation caused by earthquakes during the 2016-2017 Amatrice-Visso-Norcia seismic sequence and the Capitignano subsequence by using a boundary element method. We use rupture plane definitions from local moment tensor solutions (see supplement for solutions and dislocations). Elastic dislocations are made from earthquake rupture areas and slip that are scaled according to the empirical regressions of Wells and Coppersmith (1994), and centered at reported hypocenters/centroids. We assume that all the events occurred on the southwest-dipping nodal planes, which are the prevailing known rupture styles. Dilatation calculations are made using the subroutines of Okada (1992). Since we are calculating dilatation strain, no friction coefficient is necessary. Results are shown in Figure 5a, with much of the region showing relative negative dilatation (compression) following the seismic sequences. Additionally, we make calculations of static stress changes on the eventual Visso and Norcia mainshock ruptures utilizing available focal mechanisms of all events beginning with the Amatrice mainshock to immediately before the Visso, and then Norcia events (after Mancini et al., 2019). This is also done using the subroutines of Okada (1992), but rather than a half-space calculation, shear, normal, and Coulomb stress change calculations are resolved on the mainshock failure planes. This is done to assess the relative influence of fluid diffusion vs. direct coseismic triggering within the mainshock sequences.

Calculated changes to fluid flow directions indicate generalized migration of pore fluids away from the most negative dilatancy regions in the crust. Relative magnitudes and directions of radial flow (u_r) are calculated using Darcy's Law assuming porous flow within a confined aquifer as

$$u_r = \frac{k}{\mu}\frac{dp}{dr} \tag{8}$$

where k is the permeability of the porous rock, p is pore pressure change, r is radial distance, and μ is dynamic fluid viscosity. Here we are calculating expected relative change in subsurface flow rather than absolute values and assume that k and μ remain constant. Integrating this differential equation (e.g., Turcotte and Schubert, 1982), shows that this relation takes the form of

$$\Delta p = C \, ln\frac{r}{r_0} \tag{9}$$

where C represents assumed constants, r_0 is the position of the pressure change, and r is the location of an expected flow value at a given distance. We assume changes in dilatancy and/or normal stress are proportional to changes in pore pressure and calculate expected relative flow direction and magnitude from each cell in the model to all the others (Figure 5b).

We searched high-resolution catalogs (Tan et al., 2021) for earthquake sequences in time and space that demonstrate consistency with a diffusion signal. We found that below **M**3.5, there are too many events likely triggered through multiple processes (e.g., static stress changes, dynamic stress changes, diffusion) to reasonably identify a diffusion process. At thresholds above **M**3.5 it is possible to systematically search time windows of earthquakes sorted by time and distance from mainshocks to visually identify patterns that could represent diffusion. We then conduct least-squares regressions to see if sequences are well fit to a functional form of $d \propto t^{0.5}$, which is characteristic of fluid diffusion. These analyses do not conclusively prove the existence of a diffusion process but are used in concert with other observations such as sudden changes in attenuation, coseismic dilatation, and expected changes in fluid concentrations to demonstrate a consistent process.

4 Results

Diffusion signatures on the $Q_S^{-1}(f,t)$ time histories

Episodes of fluid diffusion are widespread in the Apennines (e.g., Malagnini et al., 2012; Miller et al., 2004). An interesting question is whether they are coupled, in a coincident fashion, with temporal variations of the attenuation parameter. Moreover, it is well known that pulses of pore-fluid pressure may trigger seismic failure by reducing a fault's shear strength. The mechanism is that the effective fault-normal stress is reduced by the counteracting effect of the fluid pressure (Terzaghi, 1923), thus reducing the fault strength (see, for example, Wang and Manga, 2010), and an interesting scientific question is whether episodes of fluid diffusion (which can possibly cause fault weakening) have detectable signatures on the attenuation parameter. Here we show cumulative evidence to support this from observed temporal changes in seismic attenuation and space-time relations amongst **M**≥3.5 earthquakes coupled with modeled crustal dilatation, fault-plane stress changes and fluid flow changes.

Following the approach developed by Malagnini et al. (2019), and Malagnini and Parsons (2020), we calculated anomalies of $Q_S^{-1}(f,t)$ from the average functional form $\langle Q_S^{-1}(f)\rangle$ calculated between 01/01/2013 and 23/08/2016/ (from the beginning of the available time window to one day before the Amatrice main shock). Results are shown in Figure 4, separated in two different time windows to minimize important effects on acausality. The $Q_S^{-1}(f,t)$ time histories after the Amatrice and Norcia mainshocks event show some consistent features: after a short-lived, sharp negative drop there is a longer positive pulse followed by a gentle negative swing. The duration of these features appears to depend on magnitude, lasting longer after the larger Norcia event. We interpret the negative anomaly as the effects of the negative dilatation documented in Figure 3 (deep decreased permeability), and the positive one as the effects of damage-like increases of the crack density (and permeability) at shallow depth.

We note that high frequency waveforms are characterized by small anomalies, indicating that what we detect in our analysis tells us something about the characteristic lengths of the shallow spatial distribution of permeability. It is well-known that below 1.0 Hz surface waves dominate the ground motion at short distance (e.g., Malagnini et al., 2000), and so the dimensions of permeability elements (clusters of interconnected cracks) affecting attenuation must be comparable with the 0.5 Hz wavelength (1-4 km). At higher frequencies we sample deeper paths because only crustal S-waves enter the calculation, and the characteristic lengths of the permeability heterogeneity distribution are smaller and comparable with the sampling wavelengths. For instance, at around 2 Hz such characteristic length may be between 0.5 and 1.5 km.

An analysis over the first 12 hours after the Amatrice main event shows three diffusion branches that follow a functional form of $d \propto t^{0.5}$ in a distance-time plot (Figure 6). Diffusion phenomena (heat or fluid diffusion equations) must have this form (see Nur and Booker, 1971; Malagnini et al., 2012). The diffusion curves are fit to a $d \propto t^{0.5}$ curve using a least squares method that finds the best fitting diffusivity constant value (r^2 values are given on the figures). The diffusion patterns are not simple (upper-left frame of Figure 6) and have also been noted by others (e.g., Tung and Masterlark, 2018; Convertito et al., 2020). Groundwater changes were also noted during and after the Amatrice mainshock (e.g., De Luca et al., 2018). As stated by Malagnini et al. (2012) for the M6.1 L'Aquila earthquake of April 6, 2009, and for the sequence of three large aftershocks that occurred on the Campotosto-Monti della Laga and Vettore-Monte Bove faults, it is likely that the tendency of the Apennines to produce diffusive episodes of crustal pore fluids inhibits large main shocks in favor of sequences of smaller events. In other words, the fault ruptures earlier in its seismic cycle. The time history of the attenuation parameter in one narrow frequency band (2 Hz) is shown in the bottom frame of Figure 6, whereas the high-frequency time history shows fluctuations of moderate amplitude, the 2-Hz waveform shows a marked decrease (to less attenuation) that lasted a bit less than 6 hours, followed by a rebound towards normal values. It is interesting that the minimum of $Q_S^{-1}(f = 2\ Hz, t)$ happens ~ 2.5 hours after the main shock, and is followed by a large positive swing less than 3 hours after the main event.

The same analysis is performed on a 10-day period starting at the onset of the Visso main event of October 26, 2016 (Figure 7). The Norcia earthquake (M_L 6.5, **M** 6.33) is also included. The 2 Hz attenuation curve is characterized by a similar behavior as after the Amatrice shock. First, at the onset of each main event, the attenuation parameter plunges steeply, then it bounces back. The time scale is about 20 times wider than that following Amatrice (Figure 6), but the negative-positive swing after each main shock takes about 24 hours to complete, which is roughly twice the time it took for the same swing after the Amatrice main event. Figure 8 shows yet another interesting situation, where a separate small seismic sequence hits the Campotosto fault (Cheloni et al., 2019; Falcucci et al., 2018; Gori et al., 2019) with a series of four **M**5+ events that occurred in less than 5 hours. The sequence migrates quickly southward along the fault with a clear diffusive signature. Potential diffusion pathways are highlighted by microseismicity from the high resolution relocated catalog of Tan et al. (2021), where fault structures are apparent in cross section view (Figure 9).

In the three cases documented in Figures 6,7,8, the diffusion coefficient is very large, up to $D \approx 2000$ m^2/sec for the faster diffusion branch activated by the Amatrice main shock (1-D diffusion). The smallest diffusion coefficient is found for the Capitignano subsequence ($D \approx 53$ m^2/sec). With the exception of the latter, whose subsequence occurred on the same Campotosto-Monti della Laga fault that saw a similar diffusion episode in 2009 with $D = 60$ m^2/sec (Malagnini et al. 2012), we find very high diffusion coefficients. We use the following equation, from Townend and Zoback (2000), to compute the rock permeability:

$$\kappa = D\eta\left(\phi\beta_f + \beta_r\right). \tag{1}$$

For a rock compressibility $\beta_r = 2 \cdot 10^{-11}$ Pa^{-1}, a fluid compressibility $\beta_f = 5 \cdot 10^{-10}$ Pa^{-1}, using a porosity $\phi = 0.05$, a viscosity $\eta = 1.9 \cdot 10^{-4}$ Pa-s, and a diffusion coefficient D in the range between 50 m^2/sec and 2000 m^2/sec (from the results shown in Figures 6,7,8), we estimate the crustal permeability along the activated fault systems to be in the range between $\kappa = 3 \cdot 10^{-13}$ m^2 and $\kappa = 1 \cdot 10^{-11}$ m^2. These estimates of rock permeability are much higher than the ones obtained for undamaged upper crust (typically between 10^{-17} m^2, and 10^{-16} m^2, Townend and Zoback, 2000), because they are relative to fresh main shock rupture zones. They are not extreme, though; for example, right after the Dobi extensional earthquake sequence in Central Afar, Noir et al. (1997) estimated a permeability $\kappa \approx 10^{-8}$ m^2.

The estimates of permeability provided above are relative to critically stressed faults that just ruptured, not to the off-fault rock matrix, where we expect that the negative dilatation due to normal-faulting earthquakes would reduce crack density and thus permeability. In other words, the values of permeability found here are relative to the crustal plumbing system in the epicentral region (fault planes outlined by the seismicity in Figure 9), in the sense described by Townend and Zoback (2000), which is contained in a volume in which the bulk permeability has decreased due to the effect of the elastic stress drop from normal faulting earthquakes (Muir-Wood and King, 1993).

Seismic attenuation occurs during propagation through bulk crustal rocks, and it is unaffected by the variations of permeability of the regional plumbing network. On the contrary, because episodes of macroscopic diffusion like those documented in Figures 6,7,8, occur along critically stressed fault planes, their parameters cannot be used to compute rocks' bulk permeabilities.

Effects of cumulative dilatation on $Q_S^{-1}(f,t)$

In the hypothesis that time-dependent seismic attenuation depends on rock permeability, we expect associations between earthquakes and changes in $Q_S^{-1}(f,t)$ to be caused by crack closure/opening induced by static stress changes from moderate-to-large events that occurred at short distances (e.g., Muir-Wood and King, 1993). We note widespread relative coseismic compression in the aftermath of mainshocks during the seismic sequence and narrower zones of dilation along fault zones (Figure 5a). During the period between the Amatrice mainshock up to the Visso event, most of the crust is under compression just south of the Visso mainshock location. Inferred fluid flow patterns suggest northward migration away from the compressed zones (and perhaps along opened fault planes) towards the Visso area as well (Figure 5b). The Visso plane is calculated to mostly have a static stress increase from the cumulative effects of prior events (Figure 10), so it is difficult to assess the relative impacts of fluid diffusion vs. static stress change triggering. Fluid flow calculations on the Visso plane based on normal stress changes where fluids are expected to migrate away from zones of clamping and into unclamped zones (assuming a sealed fault zone) do imply flow to the north towards the eventual slip zone (Figure 10).

Similarly, after the Visso mainshocks the crust around them is calculated to have a primarily compressive effect with a small gap near the Norcia mainshock (Figure 5a). Calculated fluid flow from just prior to the Norcia mainshock implies flow south towards the Norcia hypocenter as well (Figure 5b). The static stress change pattern on the Norcia rupture is complex (Figure 10) with about equal areas of Coulomb stress increase and decrease. Areas of peak slip are shown after Chiaraluce et al. (2017), which match reasonably well with the Coulomb stress increases and perhaps slightly better with changes in normal stress. Expected fluid flow changes on the fault plane from normal stress changes imply flow towards zones of greatest slip (Figure 10). The dominant postseismic signal is negative dilatation that is expected to be associated with crack closure, which causes fluids to migrate away from these regions (Figure 5b). This model is supported by water level and fluid diffusion observations that were made in the immediate periods following some of the larger earthquakes within the Amatrice-Visso-Norcia and Capitignano sequences (e.g., De Luca et al., 2018; Petitta et al., 2018). Moreover, Chiarabba et al. (2020) also supported the idea that increased fluid pressure weakened the slip patches of the fault plane of the Norcia main shock.

Discussion

Multiple physical processes are likely responsible for temporal changes in seismic attenuation, so we must thus consider multiple coseismic effects from earthquakes as we attempt to understand the observed signals that accompany seismicity. If we were to compile a list of all the things that could cause a change in Q, we would need to include many different characteristics of the specific crustal volume under investigation: thermal state, fracture density, changes in consolidation, fluid saturation, etc. Here we argue that the two most likely post-earthquake causes of fluctuations in the attenuation parameter are represented by the effects that rock dilatation (from the cumulative stress drop from the earthquakes of the sequence) and damage (from strong shaking) induce on the mobility of pore fluids within bulk rocks. Negative dilatation and damage occur simultaneously in two different ranges of depth: while dislocation-induced dilatation acts on the crustal volume around nucleation (depth~6-8 km), stress wave-induced damage is a shallow phenomenon (depth<1 km, see Kelly et al., 2013).

After a strong earthquake, we observe two competing effects of opposite signs that alternatively dominate the attenuation parameter in different time windows: damage (increase of permeability and attenuation), and increased/decreased compression (decrease/increase of permeability and attenuation). Our results indicate that the attenuation parameter $Q_S^{-1}(f,t)$ is very sensitive to fluid mobility (intra- and inter-crack) and to fluid saturation, and, together with the theoretical work by O'Connell and Budiansky (1977), strongly support the idea that seismic attenuation is intimately linked to crustal bulk (not fault) permeability. From our results, it follows that crustal permeability is modulated by variations in the compressional stress (e.g., the post-earthquake compression that occurs in normal tectonics, see Muir-Wood and King, 1993), and that fluid viscosity is the reason why a substantial portion of seismic energy goes into heat in the crust. More compression must correspond to less seismic attenuation, and vice-versa. Our analysis is extremely simple and can be summarized by just eq. (1), making artifacts very easy to spot.

Moreover, if permeability and attenuation are linked, then the sudden coseismic increases of $Q_S^{-1}(f,t)$ observed at low frequency in Figures 3 and 4 is likely the result of an increase in crack density and interconnection (permeability) associated with damage produced by the strong-motion surface waves radiated by the three main shocks of the sequence. Whereas we are unable to bring direct quantitative proof of the effects of damage, we rely on the results of other studies (e.g., Chen et al., 2015; Kelly et al., 2013; Rubinstein and Beroza, 2005). Our calculations show a sizeable and stable overall decrease in the attenuation parameter $Q_S^{-1}(f,t)$ before the seismic sequence and after the sequence ends, which corresponds to the negative cumulative dilatation caused by the elastic stress drop from the Central Apennines sequence of normal faulting earthquakes (Amatrice-Visso-Norcia, see Figure 5a). Note that the negative dilatation of Figure 5a is calculated at 5 km in depth, and that it corresponds to a reduction in the crack density of crustal rocks.

It is important to consider that we analyzed seismic attenuation at a 40 km hypocentral distance, and verified that the 1/Q variations were virtually identical at an 80 km hypocentral distance

(Figure S5), as well as at a 30 km hypocentral distance (not shown). We conclude that the observed variability over time of high-frequency observations of 1/Q must be relatively deep (hypocentral depths are 5-9 km). At frequencies f $\leq$ 1 Hz, it is likely that surface waves start dominating the seismograms (see the flattening of the average 1/Q(f) below 1.0 Hz in Figure 3d), and they sample a shallower portion of the crust. We can estimate the minimum depth by considering that we use a minimum group velocity of 1.5 km/s. At 1.0 Hz, which has a 1.5-km wavelength. A meaningful maximum value for surface-wave group velocities at 1.0 Hz could be around 3 km/s. As a rule-of-thumb, surface waves sample the crust to 1/3 of their length, and so we conclude that, at frequencies below 1 Hz, we obtain information on the attenuation between a few hundred meters and 1 km depth.

In the immediate aftermath of a mainshock, the competition between shallow rock damage and negative dilatation at depth is evident at intermediate frequencies where a short-lived increase of the parameter $Q_S^{-1}(f,t)$ is probably related to shallow rock damage, and is followed by a stable decrease of the same parameter (deeper crack closure). Zooming in on short intervals (0.5-10 days) immediately after mainshocks (i.e., Amatrice, Visso-Norcia, Capitignano), we see a consistent pattern (Figures 6,7,8). Each mainshock that initiates a sequence is associated with a sharp increase in $Q_S^{-1}(f,t)$ followed by a comparatively steep drop (Figures 6,7,8, 11, 12, and S2). We observe coincident distance (d) and time (t) behavior of **M**≥3.5 earthquakes that is consistent with fluid diffusion, where $d \propto t^{0.5}$ (Figures 6,7,8). A subsequent gradual recovery of $Q_S^{-1}(f,t)$ persists up until the next mainshock (Figure 12). We hypothesize that this recovery is associated with the redistribution of fluids into newly damaged faults and into the shallow crust where bubble production induced by traveling stress-waves may also cause significant attenuation (Tisato et al., 2015).

We argue that a dislocation-induced pressure front generated by a large earthquake and its largest aftershocks could trigger another mainshock on either a nearby fault, or on an adjacent, locked patch of the same fault. The new event could even propagate the pressure front further away, not necessarily in the same direction, starting a cascade of events. In fact, in multi-mainshock seismic sequences like the ones that struck the Apennines, multiple cycles of sudden attenuation drops, and more gentle attenuation recoveries suggest that multiple mainshocks may be triggered by intermittent episodes of fluid migration.

For example, we note that the Visso and Norcia earthquakes both lie on the same diffusion curve (Figure 7), meaning that it is possible that increased fluid pressure played a role in triggering the largest earthquake in the Central Apennines sequence. High-resolution catalogs of relocated earthquakes (e.g., Tan et al. 2021) highlight fault surfaces that likely act as high-permeability fluid pathways (Figure 9). The described mechanism could produce the occurrence of multi-mainshock sequences, in the Central Apennines as well as in any other extensional environment. As hypothesized by Malagnini et al. (2012), the induced fluid migration could also favor the segmentation of a major earthquake in multiple ruptures of smaller magnitudes.

Finally, a similar process could drive the preparatory phase of an isolated mainshock, where an individual fracture grows preferentially at the expense of the rest of the fracture population within the same crustal volume. Tectonic stress would concentrate on the growing crack, while relaxing within the adjacent crustal volume. The resulting reduction in crack porosity and the generalized closing of fractures and cracks in the volume surrounding the growing dominant fracture would cause a reduction in seismic attenuation, an increase in pore-fluid pressure, and a migration of pore fluids. The process would culminate with the occurrence of the first main shock.

Open questions:

1. Why is crustal attenuation extremely sensitive to bulk compression/dilatation? Malagnini et al., (2019) used the results by Johnson et al. (2017) and demonstrated that, at 2-4 km in depth on the SAF at Parkfield, the attenuation parameter responds to normal stress cyclic anomalies across the fault of the order of ~ 100 Pa. The extreme sensitivity indicates that it is the ground motion noise that dominates the random fluctuations that affect our measurements, and not fluctuations of the physical properties of crustal rocks. Once we reduce the noise to a sufficiently low level, we only see the fluctuations of rock permeability. This demonstrates that other physical properties of crustal rocks are very stable over time. This is especially important for analyzing the effects of long-period stress periodicities, like the ones associated with seasonal loading and unloading from precipitation, multi-year wet-dry cycles, the polar tide, or solid Earth tides with multiple and submultiple periods of 28 days.

2. The most important aspect of this research is the potential use of our results for monitoring purposes, where precursory phenomena of large earthquakes might be detected. In fact, the evolution of the crustal crack distribution yields information about variations in strength of some portions of the crust under mounting tectonic stress, where stress tends to concentrate before a crustal rupture. If observed fluctuations of the attenuation parameter are directly linked to variations in the crack density, the latter must be in direct connection with variations of strength.

We note that Italy already has a high-quality seismic network (the Rete Sismica Nazionale, RSN). If the station density of the RSN was improved by an order of magnitude, we would be able to monitor the variability of the attenuation parameter of small regions of specific interest. At least, it would become possible to monitor localized anomalies in the attenuation parameter. Borehole stations would allow a much lower magnitude threshold than the one used here $(M \geq 2)$ for high-quality recordings of small earthquakes, allowing a finer spatial and temporal resolution in our monitoring purposes.

A much denser seismic network made of borehole instruments could produce a huge volume of high-quality recordings, and AI algorithms would have to be developed for the quality control of the recorded waveforms. They could be run in quasi-real time, in parallel with multi-frequency sets of regressions like the one presented here. The goal would be to use such tools to locate attenuation anomalies in space and time, in a quest for precursory phenomena.

5 Conclusions

The characteristics of the attenuation parameter (Figures 3, 4, 11, and 12) confirm the conceptual model formulated by Malagnini and Parsons (2020), that the time variations in rock permeability modulate the variability of the attenuation parameter. In fact, Figures 3d and 4 show that the average level of the background attenuation parameter between January 2013 and immediately prior to the onset of the sequence, on August 24, 2016, is higher than the background value after the sequence. Figure 5a shows that the cumulative effect of the seismic sequence (the multiple main shocks) on the study area was a negative dilatation (relative increase in compression); such an effect favored crack closure, and thus a decrease in permeability, and in anelastic attenuation as well.

The Central Apennines is a region under extensional tectonics, prone to multi-mainshock seismic sequences behaving like a cascade of several mainshocks: for example the 2016-2017 seismic sequence studied here, the Umbria-Marche sequence (swarm) of 1997-1998 (Miller et al., 2004; Amato et al., 1998), and the episode that occurred during the 2009 L'Aquila-Campotosto-Monti della Laga sequence (Malagnini et al., 2012).

Here we propose a possible physical mechanism for a cascade of multiple main shocks under extensional tectonics. We envision two main phases: 1) a pre-seismic phase that lasts up to the first earthquake and 2) intermediate phases, which may be cycled through several times, one for each subsequent main shock. In the first phase, the dilatancy model (Scholtz, 2019) predicts that at some point the preferential growth of one fracture takes place at the expense of the general population of cracks that tend to close during this preliminary phase. Such behavior must have consequences on pore fluid pressure, which changes as stress affects cracks. Pore-fluid drops imply fault strengthening, and inhibit rupture. Conversely, pore-fluid pressure rises imply fault weakening, and promote rupture. In the intermediate phases that start at mainshock onsets, two main physical processes compete in defining the attenuation parameter, rock permeability and, consequently, pore-fluid pressure. These processes are damage and negative dilatation (stress drop). While damage would correspond to a drop in pore-fluid pressure in the shallow crust, negative dilatation and healing correspond to a deeper pore-pressure rise.

Muir-Wood and King (1993) observed that, in an extensional environment, the seismic stress drop of a main event always increases stream discharge, up to an order of magnitude more in volume than a reverse-fault mainshock of the same magnitude. This is because the elastic stress drop tends to close cracks oriented orthogonally to the (horizontal) direction of the minimum principal stress, causing a sudden increase in the pore-fluid pressure. A similar crack closure (pressure rise) may be envisioned in the pre-seismic phase, in which dilatancy predicts the preferential growth of one crack that is favorably oriented to the stress field, at the expense of the general population of cracks that during this preliminary phase tends to close.

Our conceptual model may be described as follows:

1. During the pre-seismic rupture growth in an extensional environment there may be a “*slow*” localized negative dilatation, crack closure, pore-pressure rise and migration (diffusion) along fault, and a resulting decreased fault strength that leads to the first main rupture. In all that we describe, permeability must be low enough to support local pore pressure increases, probably over a time scale of several weeks or months.
2. The first main event produces coseismic damage and negative dilatation: while the first causes a fluid pressure drop (short-lived), the second causes a fluid pressure rise (persistent); $1/Q_S$ shows opposite behavior. In turn, the fluid pressure rise and migration (diffusion) is responsible for the strength reduction in nearby faults, and the occurrence of the next earthquake. The cycling over a number of cascading main events ends when the system is depleted of its elastic energy below a certain threshold, when it is not able to produce any more ruptures.

Acknowledgments, Samples, and Data

Funding:

Progetti INGV di Ricerca Libera 2019 (LM), Progetto INGV "Pianeta Dinamico" (LM), Centro di Pericolosità Sismica, Triennio 2019-2021 Convenzione B1 Dipartimento della Protezione Civile – INGV (IM).
Competing interests: Authors declare that they have no competing interests

Data and materials availability: All seismometric data are available at the European Integrated Data Archives (EIDA, https://www.orfeus-eu.org/data/eida/); all accelerometric data are available at the ITACA data center (http://itaca.mi.ingv.it/ItacaNet_31/#/home).

References

1. Akinci E. Del Pezzo, and L. Malagnini (2020). Seismic Wave Attenuation and Scattering in the Central Apennines (Italy), *Physics of the Earth and Planetary Interiors*, https://doi.org/10.1016/j.pepi.2020.106498.
2. Amato, A., et al. (1998). The 1997 Umbria-Marche, Italy, earthquake sequence: A first look at the main shocks and aftershocks, *Geophys. Res. Lett.*, **25**, 2861– 2864.
3. D.M. Boore, and W.B. Joyner (1984). A note on the use of random vibration theory to predict peak amplitudes of transient signals, *Bull. Seism. Soc. Am*. 74 (5): 2035–2039.
4. Brodsky, E.E, E. Roeloffs, D. Woodcock, I. Gall, and M. Manga (2003). A mechanism for sustained groundwater pressure changes induced by distant earthquakes. *J. Geophys. Res.* 108, 2390.
5. Barbosa, N.D., J. Hunziker, S. Lissa, E.H Saenger, and M. Lupi (2019). Fracture unclogging: A numerical study of seismically induced viscous shear stresses in fluid-saturated fractured rocks, J. Geophys. Res., 124, 11, pp 11705-11727, https://doi.org/10.1029/2019JB017984.
6. Cartwright, D.E., and M.S. Longuet-Higgins (1956). The statistical distribution of the maxima of a random function, *Proc. R. Soc. Lond. A*, 237**,** 212–232, https://doi.org/10.1098/rspa.1956.0173.
7. Cheloni, D., N. D'Agostino, L. Scognamiglio, E. Tinti, C. Bignami, A. Avallone, R. Giuliani, S. Calcaterra, P. Gambino, and M. Mattone (2019). Heterogeneous behavior of the Campotosto normal fault (Central Italy) imaged by InSAR GPS and Strong-Motion Data:

Insights from the 18 January 2017 events, Remote Sens. 2019, 11, 1482, doi: 10.3390/rs11121428.

8. Chen, K.H., T. Furumura, and J. Rubinstein (2015). Near-surface versus fault zone damage following the 1999 Chi-Chi earthquake: Observation and simulation of repeating earthquakes, J. Geophys. Res., 120, 4, 2426-2445, https://doi.org/10.1002/2014JB011719.

9. Chiarabba, C., De Gori, P., Segou, M., and Cattaneo, M., 2020, Seismic velocity precursors to the 2016 Mw 6.5 Norcia (Italy) earthquake: Geology, v. 48 (9): 924-928, https://doi.org/10.1130/G47048.1.

10. Chiarabba, C., D. Piccinini, and P. De Gori (2009), Velocity and attenuation tomography of the Umbria Marche 1997 fault system: Evidence of a fluid-governed seismic sequence https://doi.org/10.1016/j.tecto.2009.04.004

11. Chiaraluce, L., R. Di Stefano, E. Tinti, L. Scognamiglio, M. Michele, E. Casarotti, M. Cattaneo, P. De Gori, C. Chiarabba, G. Monachesi, A. Lombardi, L. Valoroso, D. Latorre, and S. Marzorati (2017), The 2016 Central Italy Seismic Sequence: A First Look at the Mainshocks, Aftershocks, and Source Models, Seismological Research Letters, 88, 757-771, doi: 10.1785/0220160221.

12. Convertito V, De Matteis R, Improta L and Pino NA (2020), Fluid-Triggered Aftershocks in an Anisotropic Hydraulic Conductivity Geological Complex: The Case of the 2016 Amatrice Sequence, Italy, Front. Earth Sci. 8:541323, doi: 10.3389/feart.2020.541323.

13. De Luca, G., G. Di Carlo, and M. Tallini (2018), A record of changes in the Gran Sasso groundwater before, during and after the 2016 Amatrice earthquake, central Italy, Scientific Reports, 8:15982, DOI:10.1038/s41598-018-34444-1.

14. Falcucci, E., S. Gori, C. Bignami, G. Pietrantonio, D. Melini, M. Moro, M. Saroli, and F. Galadini (2018). The Campotosto seismic gap in between the 2009 and 2016-2017 seismic sequences of Central Italy and role of inherited lithospheric faults in regional

seismotectonic settings, *Tectonics*, 37, 2425-2445. https://doi.org/10.1029/2017TC004844.

15. Gori, S., I. Munafò, E. Falcucci, M. Moro, M. Saroli, L. Malagnini, and F. Galadini (2019). Active faulting and seismotectonics in central Italy: lesson learned from the past 20 years of seismicity. Engineering clues, Earthquake Geotechnical Engineering for Protection and Development of Environment and Constructions-Silvestri & Moraci (Eds), ISBN 978-0-367-14328-2.

16. Hoshiba, M. (1995). Estimation of nonisotropic scattering in western Japan using coda wave envelopes' Application of a multiple nonisotropic scattering model, *J. Geophys. Res.* 100, B1, 645-657.

17. Kelly, C. M., A. Rietbrock, D. R. Faulkner, and R. M. Nadeau (2013). Temporal changes in attenuation associated with the 2004 M6.0 Parkfield earthquake*, J. Geophys. Res. Solid Earth,* 118, 630–645, doi:10.1002/jgrb.50088.

18. Kilb, D., G. Biasi, J. Anderson, J. Brune, Z. Peng, and F.L. Vernon (2012). A Comparison of Spectral Parameter Kappa from Small and Moderate Earthquakes Using Southern California ANZA Seismic Network Data, *Bull. Seism. Soc. Am.,* 102 (1): 284–300, https://doi.org/10.1785/0120100309.

19. Johanson, I. A., and R. Bürgmann (2010), Coseismic and postseismic slip from the 2003 San Simeon earthquake and their effects on backthrust slip and the 2004 Parkfield earthquake, *J. Geophys. Res,.* **115**, B07411, doi:10.1029/2009JB006599.

20. Johnson, C. W., Fu, Y., and R. Bürgmann (2017). Stress models of the annual hydrospheric, atmospheric, thermal, and tidal loading cycles on California faults: Perturbation of background stress and changes in seismicity. *J. Geophys. Res. Solid Earth,* 122, 10,605–10,625. https://doi.org/10.1002/2017JB014778

21. Liu, W., and M. Manga (2009). Changes in permeability caused by dynamic stresses in fractured sandstone*, Geophys. Res. Lett.,* 36, L20307, doi:10.1029/2009GL039852.

22. O'Connell, R. J., and B. Budiansky (1977), Viscoelastic properties of fluid-saturated cracked solids, J. Geophys. Res., 82, 5719-5735.

23. Malagnini, L., and T. Parsons (2020). Seismic attenuation monitoring of a critically stressed San Andreas fault, *Geophys. Res. Lett.,* https://doi.org/10.1029/2020GL089201.

24. Malagnini, L., Dreger, D. S., Bürgmann,R., Munafò, I., & Sebastiani, G. (2019). Modulation of seismic attenuation at Parkfield, before and after the 2004 M6 earthquake. *J. Geophys. Res.*: Solid Earth,124, 5836–5853. https://doi.org/10.1029/2019JB017372.

25. Malagnini, L., and D.S. Dreger (2016). Generalized Free-Surface Effect and Random Vibration Theory: a new tool for computing moment magnitudes of small earthquakes using borehole data, *Geophys. J. Int.,* **206**, 103-113. doi: https://doi.org/10.1093/gji/ggw113.

26. Malagnini, L., F. Lucente, P. De Gori, A. Akinci, and I. Munafo' (2012). Control of Pore-Fluid Pressure Diffusion on Fault Failure Mode: Insights from the 2009 L'Aquila Seismic Sequence, J. Geophys. Res. 117, ISSN: 0148-0227, doi: 10.1029/.2011JB008911.

27. Malagnini, L., A. Akinci, K. Mayeda, I. Munafo', R.B. Herrmann, and A. Mercuri (2011). Characterization of Earthquake-Induced Ground Motion from the L'Aquila Seismic Sequence of 2009, Italy, Geophys. J. Int., Geophys. J. Int. 184, 325–337, DOI: 10.1111/j.1365-246X.2010.04837.x.

28. Malagnini, L., Herrmann, R.B., and M. Di Bona (2000). Ground motion scaling in the Apennines (Italy). *Bull. Seism. Soc. Am*.,90, 1062-1081.

29. Mancini, S., M. Segou, M. J. Werner, and C. Cattania (2019), Improving physics-based aftershock forecasts during the 2016-2017 central Italy earthquake cascade, J. Geophys. Res. 124, doi:10.1029/2019JB017874.

30. Manga,M., I. Beresnev, E. E. Brodsky, J. E. Elkhoury, D. Elsworth, S. E. Ingebritsen, D. C. Mays, and C.-Y.Wang (2012), Changes in permeability caused by transient stresses: Field observations, experiments, and mechanisms, Rev. Geophys., 50, RG2004, doi:10.1029/2011RG000382.

31. Manga, M., and E. Brodsky, Seismic triggering of eruptions in the far field: Volcanoes and geysers. Annu. Rev. Earth Planet. Sci. 34, 263–291 (2006).
32. Miller, S., Collettini, C., Chiaraluce, L. *et al.* (2004). Aftershocks driven by a high-pressure CO_2 source at depth. *Nature* **427,** 724–727, https://doi.org/10.1038/nature02251.
33. Mitchell, B.J. (1995). Anelastic structure and evolution of the continental crust and upper mantle from seismic surface wave attenuation, Reviews of Geophysics, 33, 4, 441-462, https://doi.org/10.1029/95RG02074.
34. Muir-Wood, R., and G.C.P. King (1993). Hydrological Signatures of Earthquake Strain, J. Geophys. Res., 98, B12, 22035-22068.
35. Noir, J., E. Jacques, S. Békri, P. M. Adler, P. Tapponnier, and G. C. P. King (1997). Fluid flow triggered migration of events in the 1989 Dobi Earthquake sequence of central Afar, Geophys. Res. Lett., 24(18), 2335–2338, doi:10.1029/97GL02182.
36. Nur, A., and J. R. Booker (1971). Aftershocks Caused by Pore Fluid Flow?, Science, 175, 885-887, doi: 10.1126/science.175.4024.885.
37. Parsons, T., L. Malagnini, and A. Akinci (2017). Nucleation speed limit on remote fluid-induced earthquakes, Science Advances, Sci. Adv. 3 (8), e1700660, https://doi.org/10.1126/sciadv.1700660.
38. Petitta, M., L. Mastrorillo, E. Preziosi, F. Banzato, M.D. Barberio, A. Billi, C. Cambi, G. De Luca, G. Di Carlo, D. Di Curzio, C. Di Salvo, T. Nanni, S. Palpacelli, S. Rusi, M. Saroli, M. Tallini, A. Tazioli, D. Valigi, P. Vivalda, and C. Doglioni (2018). Water-table and discharge changes associated with the 2016–2017 seismic sequence in central Italy: hydrogeological data and a conceptual model for fractured carbonate aquifers. *Hydrogeol J* **26,** 1009–1026. https://doi.org/10.1007/s10040-017-1717-7
39. Raoof, M., R.B. Herrmann, and L. Malagnini (1999). Excitation of three-component ground motion in Southern California, Bull. Seism. Soc. Am., 89, 888-902.
40. Roeloffs (1998). Persistent water level changes in a well near Parkfield, California, due to local and distant earthquakes, J. Geophys. Res., 103 B1, 869-889.

41. Rubinstein, J. L. and G. C. Beroza (2005), Depth Constraints on Nonlinear Strong Ground Motion from the 2004 Parkfield Earthquake, GRL, vol. 32, L14313, doi: 10.1029/2005GL023189.

42. Scholz, C. (2019). *The Mechanics of Earthquakes and Faulting*. Cambridge: Cambridge University Press. doi:10.1017/9781316681473.

43. Silverii, F., N. D'Agostino, A.A. Borsa, S, Calcaterra, P. Gambino, R. Giuliani, M. Mattone (2018). Transient crustal deformation from karst aquifers hydrologyi n the Apennines (Italy), Earth Planet. Sci. Lett., 506, 23–37, https://doi.org/10.1016/j.epsl.2018.10.019.

44. Tan, Y. J., F. Waldhauser, W. L. Ellsworth, M. Zhang, W. Zhu, M. Michele, L. Chiaraluce, G. C. Beroza, and M. Segou (2021), Machine-Learning-Based High-Resolution Earthquake Catalog Reveals How Complex Fault Structures Were Activated during the 2016–2017 Central Italy Sequence, The Seismic Record, 1, 11–19, https://doi.org/10.1785/0320210001

45. Terzaghi, K. (1923). Die Berechnung der Durchassigkeitsziffer des Tones aus dem Verlauf der hydrodynamischen Spannungsercheinungen*, Sitzungsber. Akad. Wiss. Wien Math. Naturwiss. Kl.*, Abt. 2A, 132, 105-124, 1923.

46. Tinti, E., P. Spudich, and M. Cocco (2005). Earthquake fracture energy inferred from kinematic rupture models on extended faults, J. Geophys. Res., 110, B12303, doi:10.1029/2005JB003644.

47. Tisato, N., B. Quintal, S. Chapman, Y. Podladchikov, J-P. Burg (2015). Bubbles attenuate elastic waves at seismic frequencies: First experimental evidence, Geophys. Res. Lett. 42, 3880-3887, https://doi.org/10.1002/2015GL063538.

48. Titzschkau, T., M. Savage, and T. Hurst (2010). Changes in attenuation related to eruptions of Mt. Ruapehu Volcano, New Zealand, Journal of Volcanology and Geothermal Research, 190, 1–2, pp. 168-178, https://doi.org/10.1016/j.jvolgeores.2009.07.012.

49. Townend, J., and M.D. Zoback (2000). How faulting keeps the crust strong, GEOLOGY, 28 (5): 399.

50. Tung, S., and Masterlark, T. (2018). Delayed poroelastic triggering of the 2016 October Visso earthquake by the August Amatrice earthquake, Italy. Geophysical Research Letters, 45, 2221–2229. https://doi.org/10.1002/2017GL076453

51. Wang, C.-Y., and M. Manga (2010). Hydrologic responses to earthquakes and a general metric, *Geofluids* (2010) **10**, 206–216, https://doi.org/10.1111/j.1468-8123.2009.00270.x.

52. Wells, D. L., and K. J. Coppersmith (1994), New empirical relationships among magnitude, rupture length, rupture width, rupture area, and surface displacement, Bull. Seismol. Soc. Am., 84, 974– 1002.

53. Winker, K.W. and A. Nur (1982). Seismic attenuation: Effects of pore fluids and frictional-sliding, *Geophysics,* 47, 1-15, https://doi.org/10.1190/1.1441276.

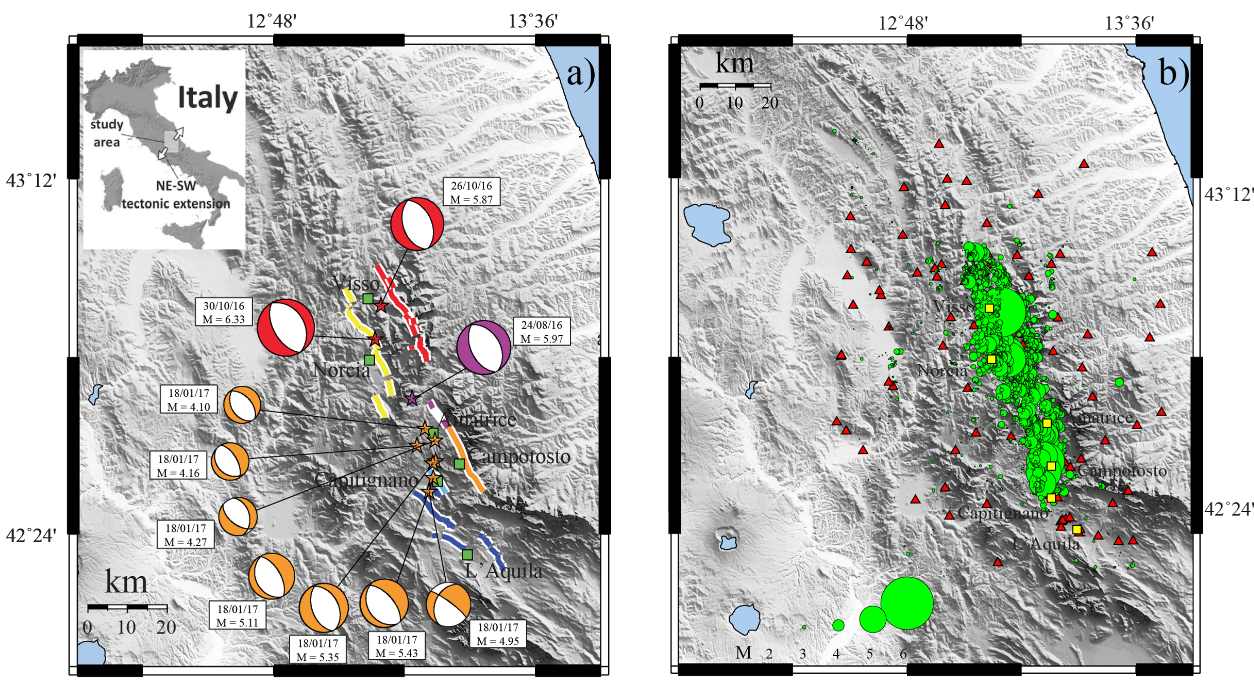

Figure 1. Representation of the data set. a) Mechanisms of selected earthquakes, including the mainshocks of the Amatrice, Visso and Norcia and the major seven events of Capitignano sequence (from http://eqinfo.eas.slu.edu/eqc/eqc_mt/MECH.IT/). Fault traces are represented by colored lines (fault strands with the same color pertain to the same seismogenic fault system, from Gori et al., 2019). Fault systems are matched with the corresponding focal solutions using the same color; stars correspond to the location of the mainshocks, whereas white squares represent the main cities of the area. **b)** Locations and magnitudes of the 3,236 earthquakes used

in this study (2.0 < **M** < 6.33) occurred in the time window between 07/01/2013 and 31/08/2020; gray squares indicate the main cities of the area.

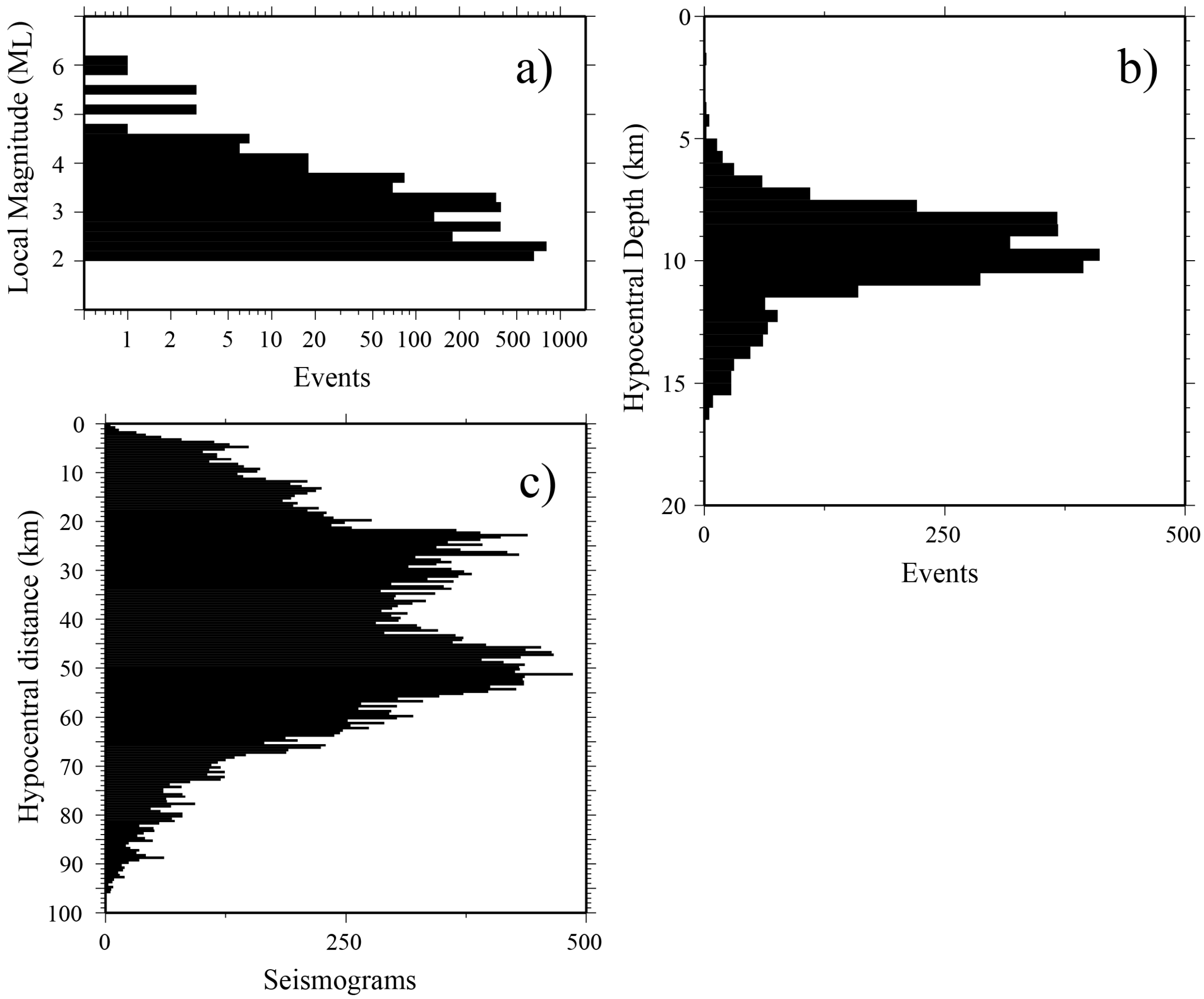

Figure 2. Histograms describing our data set: **a)** local magnitudes (M_L); **b)** hypocentral depths; **c)** source-receiver hypocentral distances.

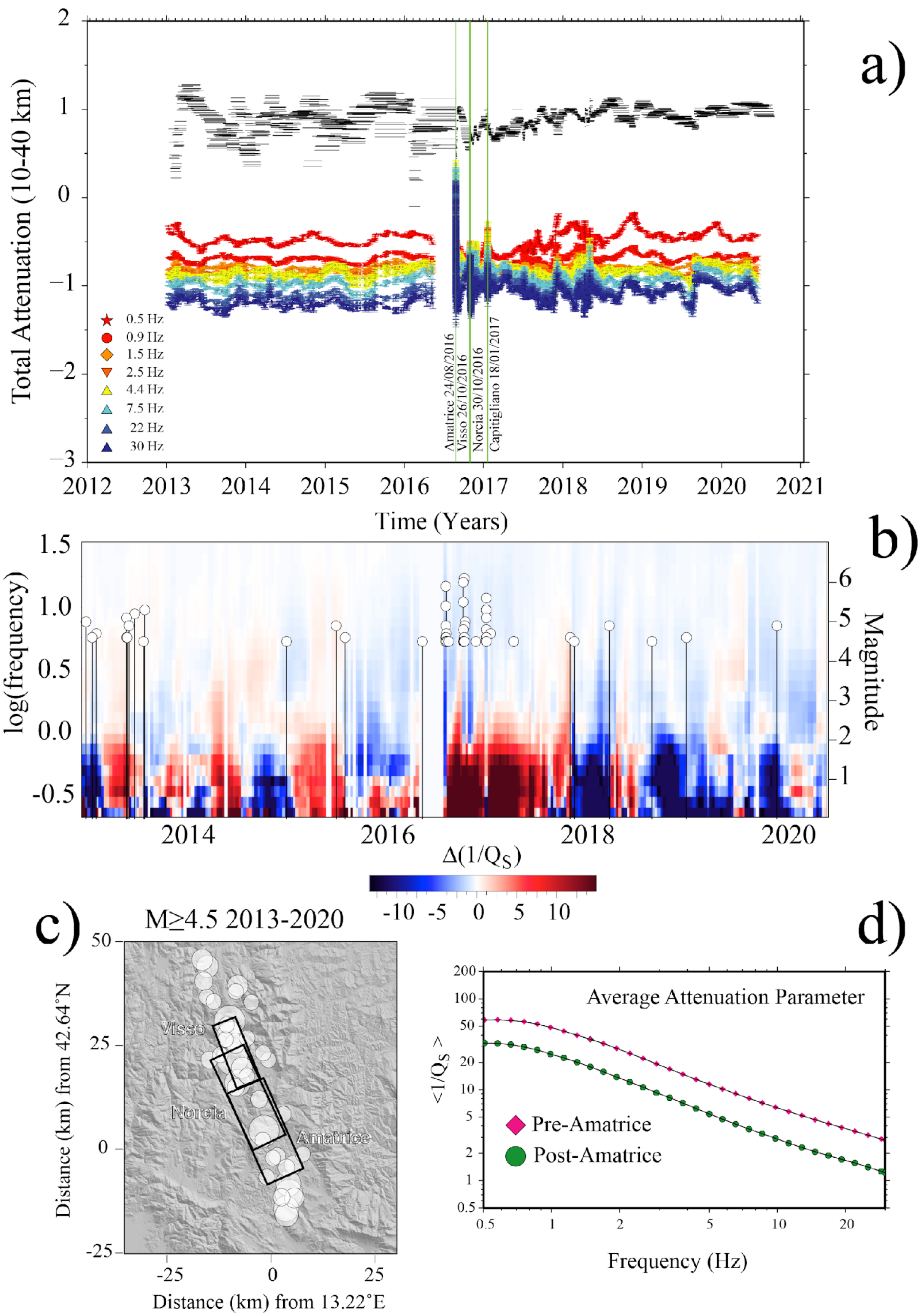

1005

1006 **Figure 3. a)** Colored symbols: total attenuation (geometric and anelastic) calculated between 10
1007 and 40 km of hypocentral distance in the Central Apennines, before, during, and after the 2016-
1008 2017 sequence. Horizontal black segments: durations of each one of the *m* time windows (each

one contains 40 events) used to scan the entire period (horizontal black segments. Indicated are the main shocks of Amatrice, Visso and Norcia. Malagnini et al. (2019) and Malagnini and Parsons (2020) hypothesized that the fluctuations of $Q_S^{-1}(t,f)$ over time as linked to stress-induced fluctuations of crack density and connectivity. That is, to variations of rock permeability. Within such a hypothesis, earthquake-generated stress waves induce cyclic movements of rock fluids through variable compressions of the cracked rock matrix. Along permeable paths of interconnected cracks, seismic waves induce fluid flows of lengths comparable to their wavelengths: high-frequency seismic waves act only on comparatively short paths of interconnected cracks, low-frequency seismic waves can affect longer paths, and the two situation would be differently efficient in attenuating seismic waves, because although they would be dominated by different loading times, the circulating fluid would be the same, and its viscosity would be constant. **b)** Two-D representation of the attenuation parameter $Q_S^{-1}(t,f)$, which indicated the magnitudes and times of occurrence of events with **M**≥4.5. The frequency axis is in log scale. **c)** Epicentral locations of the events with **M**≥4.5 indicated in **b)**. Rectangles indicate the approximate ruptures of the three main shocks of the sequence. **d)** Time-averaged attenuation parameters $\langle Q_S^{-1}(f)\rangle$ calculated in the pre-Amatrice time window (January 07 2013 through August 23 2016, red symbols), and in the post-Amatrice one (August 24 2016 through August 20 2020, green symbols).

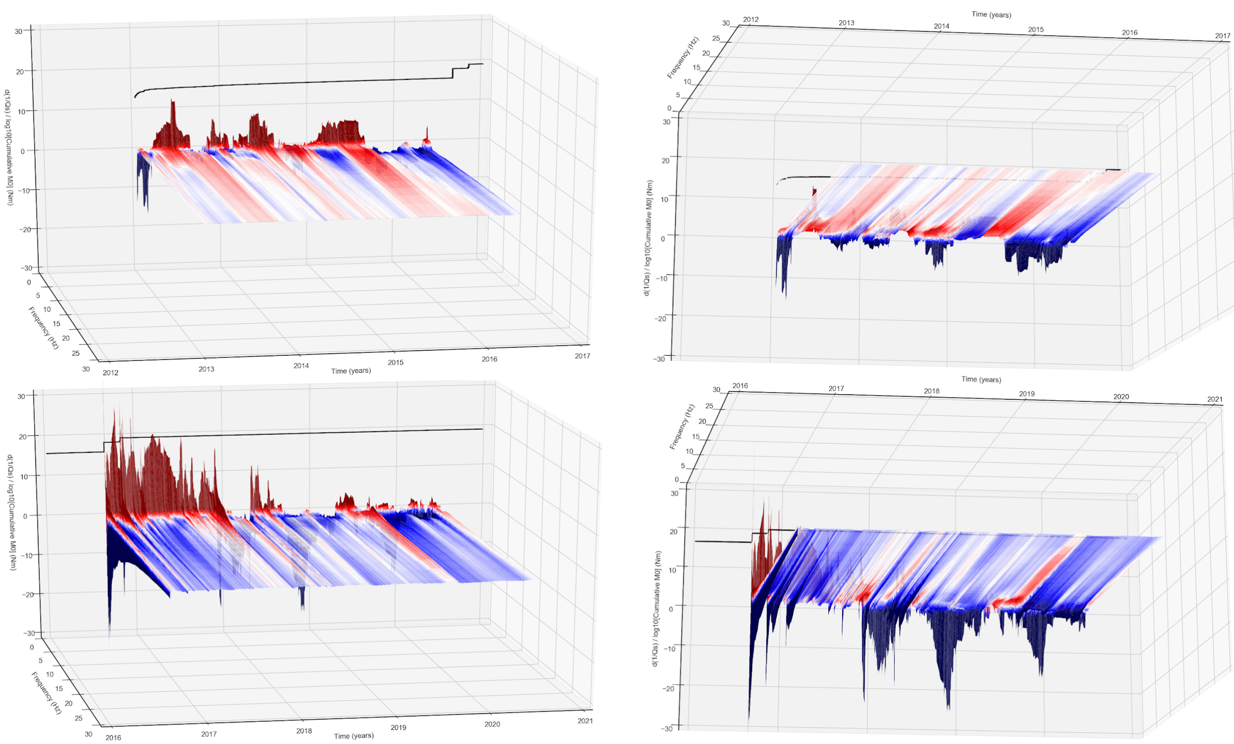

Figure 4. Seismic attenuation as a function of time and frequency, calculated at a hypocentral distance of 40 km. Central Apennines, before and after the Amatrice main shock of August 24, 2016. **Upper:** from two different points of view, anomalies of $Q_S^{-1}(f,t)$ from the average calculated between 01/01/2013 and 23/08/2016 (one day before the Amatrice main shock). **Lower:** from two different points of view, anomalies of $Q_S^{-1}(f,t)$ from the average calculated as described above, in the time window starting at the onset of the Amatrice main shock. After the

first main shock of the Amatrice sequence (M6, 24/08/2016), the seismic parameter in the epicentral region undergoes an instantaneous drop due to the coseismic stress drop-induced negative dilatation. The latter produces a sudden reduction of the crustal bulk permeability via a reduction of crack density and interconnection. The strong ground shaking is responsible for a contrasting action that tends to increase crack density in rocks that are very close to the free surface through damage (Rubinstein and Beroza, 2005; Kelly et al. 2013; Malagnini et al., 2019). Damage produces the positive peaks that affect the attenuation parameter at low-frequency (say, below 2.0 Hz), that occur immediately after the negative anomalies discussed earlier. Damage probably also produces the thin “lines” of increased attenuation parameter that can be seen after each main shock (see Figure 11). Because low-frequency shaking is associated with surface waves, in such a portion of the spectrum, damage is the dominant effect over reduction of crack density and permeability produced by the coseismic stress drop.

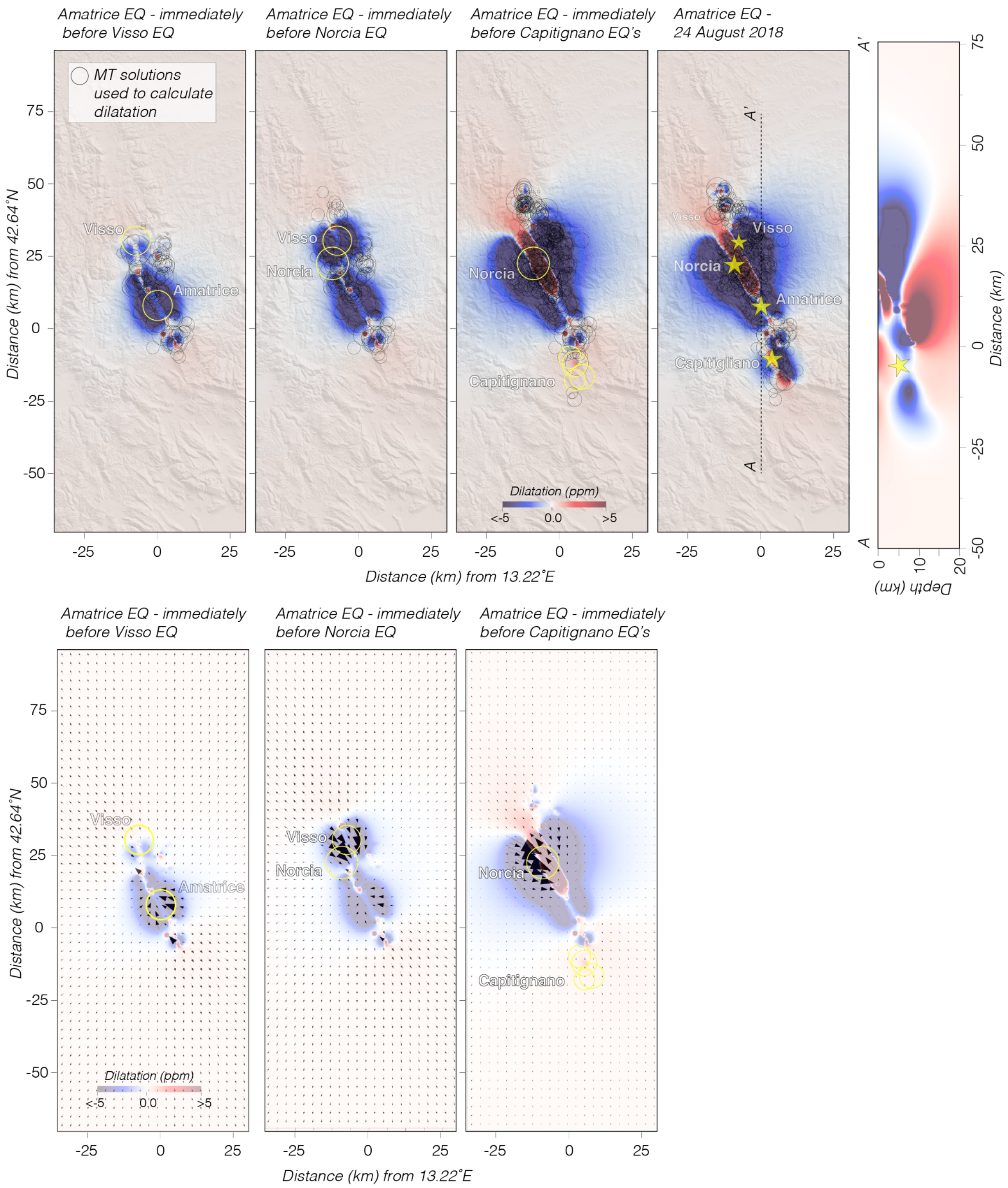

Figure 5. a) Cumulative dilatation. Cumulative dilatation is calculated assuming the SW dipping moment tensor solutions of M≥3 earthquakes were the rupture planes. Dilatation is shown on horizontal planes at 5 km depth, and a cross section is also shown. If drops in $Q_S^{-1}(f,t)$ are related to drops in crack density, negative dilatation (compression) is to be expected, in close agreement with the conceptual model by Muir-Wood and King (1993). **b)** Expected relative flow magnitudes and directions resulting from coseismic dilatation

changes caused by M≥3 earthquakes beginning with the 24 August 2016 Amatrice earthquake to times just before the Visso, Norcia, and Capitignano earthquakes.

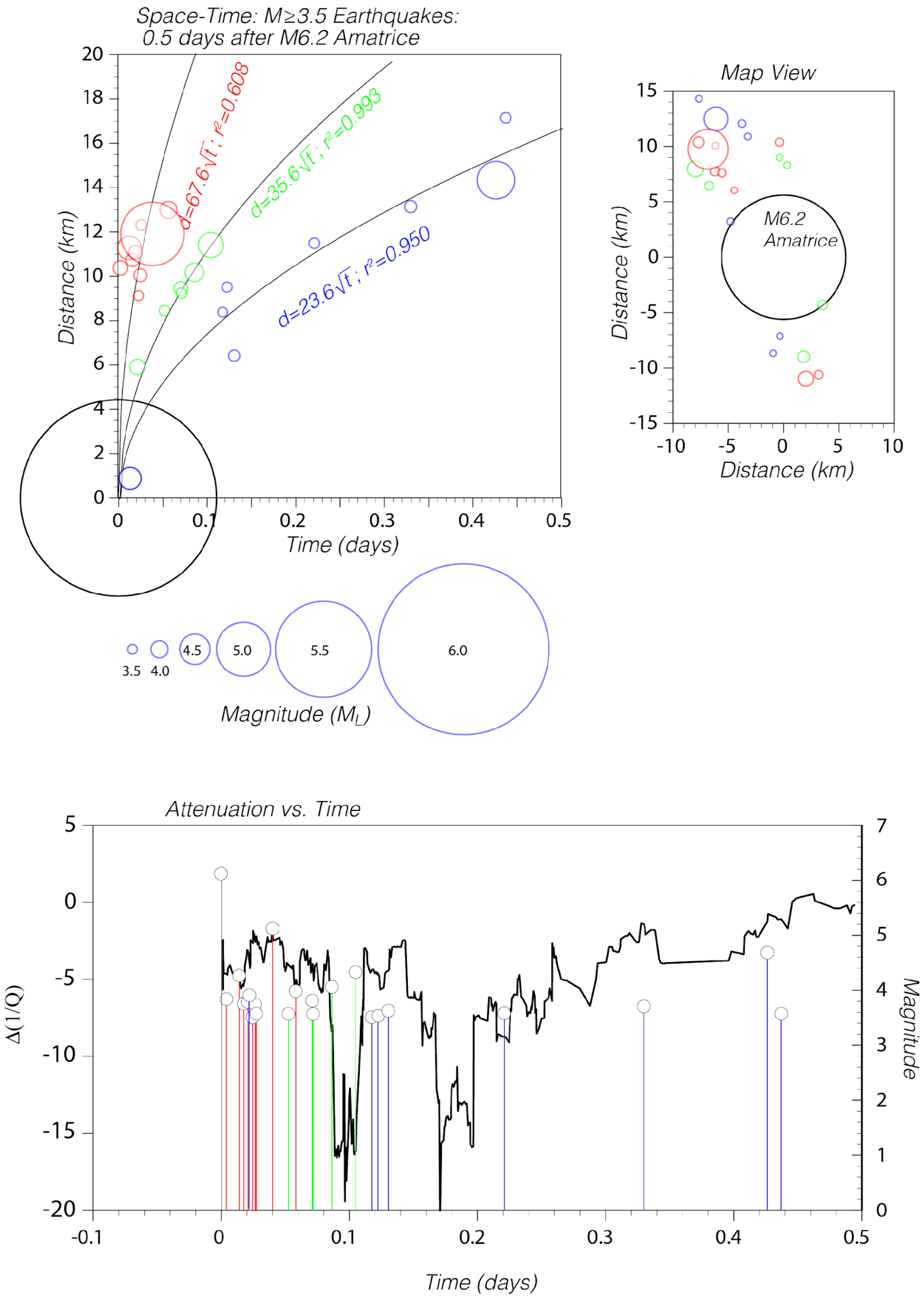
Space-Time: M≥3.5 Earthquakes:
0.5 days after M6.2 Amatrice
d=67.6√t ; r²=0.608
d=35.6√t ; r²=0.993
d=23.6√t ; r²=0.950
Distance (km)
Time (days)
3.5
4.0
4.5
5.0
5.5
6.0
Magnitude (ML)
Map View
M6.2
Amatrice
Distance (km)
Distance (km)
Attenuation vs. Time
Δ(1/Q)
Magnitude
Time (days)

Figure 6. Diffusion and attenuation vs. time: Amatrice. Upper: three different simultaneous diffusion processes may be recognized mostly to the North of the Amatrice main shock. Map view to the right. **Lower:** 2.2 Hz seismic attenuation (black solid line) drops for about six hours after the mainshock, then goes back to higher values (still negative). The drop in attenuation may be associated to the effect of the coseismic stress drop on the crustal cracks (coseismic crack closure is expected in normal-faulting earthquakes, see Muir-Wood and King, 1993) and thus to crustal permeability. Over a broader time window, the effects are clear and may be interpreted in terms of two competing effects: damage of shallow crustal rocks (Rubinstein and Beroza, 2005), and crack closure due to the coseismic stress drop of a normal-faulting earthquake. The colors of the vertical lines associated with earthquakes correspond with the earthquakes portrayed by colored circles in the upper panel.

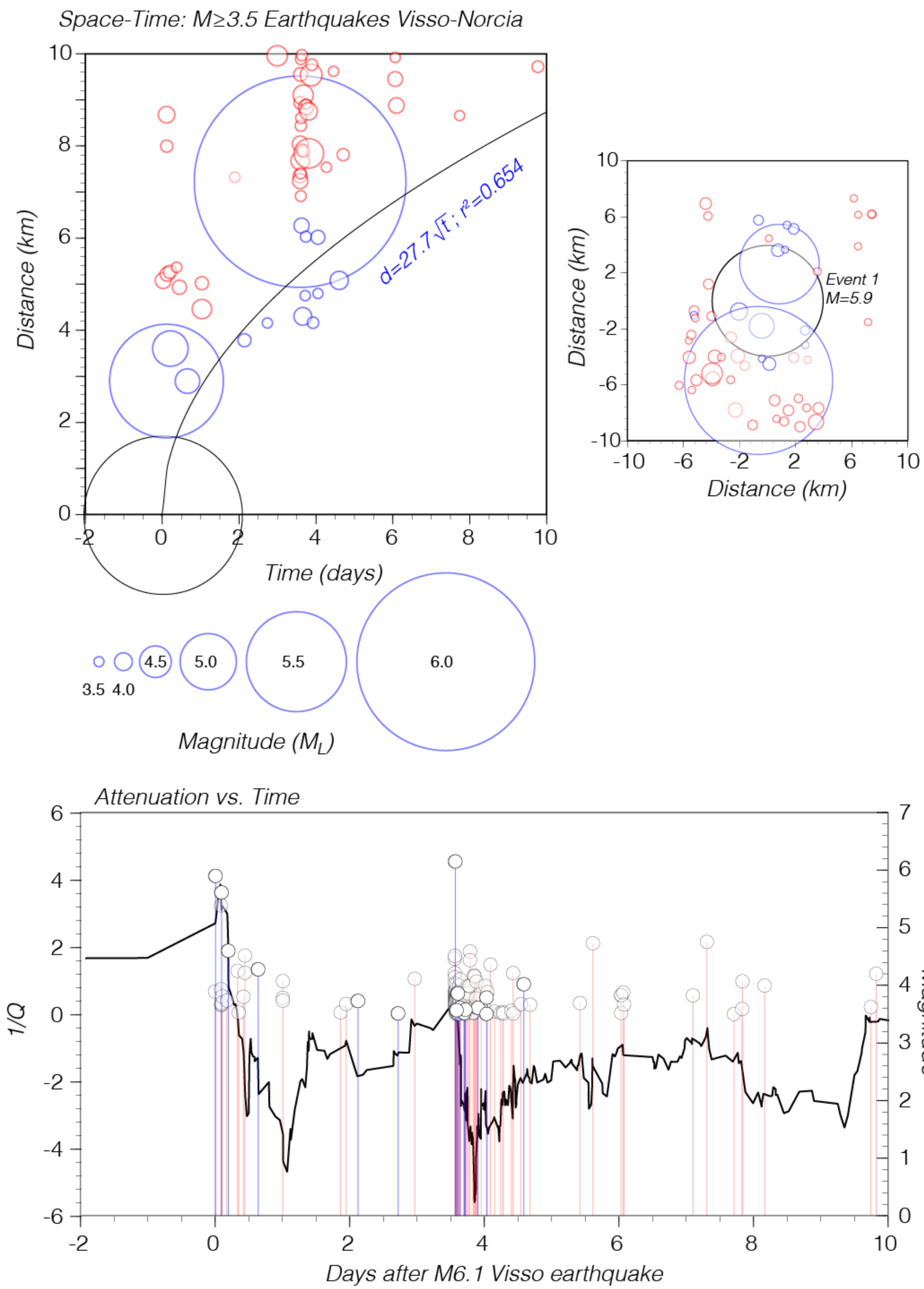
Space-Time: M≥3.5 Earthquakes Visso-Norcia
Distance (km)
Time (days)
d=27.7 √t ; r²=0.654
Event 1
M=5.9
Distance (km)
Distance (km)
3.5
4.0
4.5
5.0
5.5
6.0
Magnitude (M_L)
Attenuation vs. Time
1/Q
Magnitude
Days after M6.1 Visso earthquake

Figure 7. Diffusion and attenuation vs. time: Visso-Norcia. Upper: diffusion process associated to the mainshocks of Visso (October 26, 2016) and Norcia (October 30, 2016), with a map view to the right. **Lower:** 2.2 Hz fluctuation of the seismic attenuation parameter around the pre-Amatrice average. The colors of the vertical lines associated with earthquakes correspond with the earthquakes portrayed by colored circles in the upper panel.

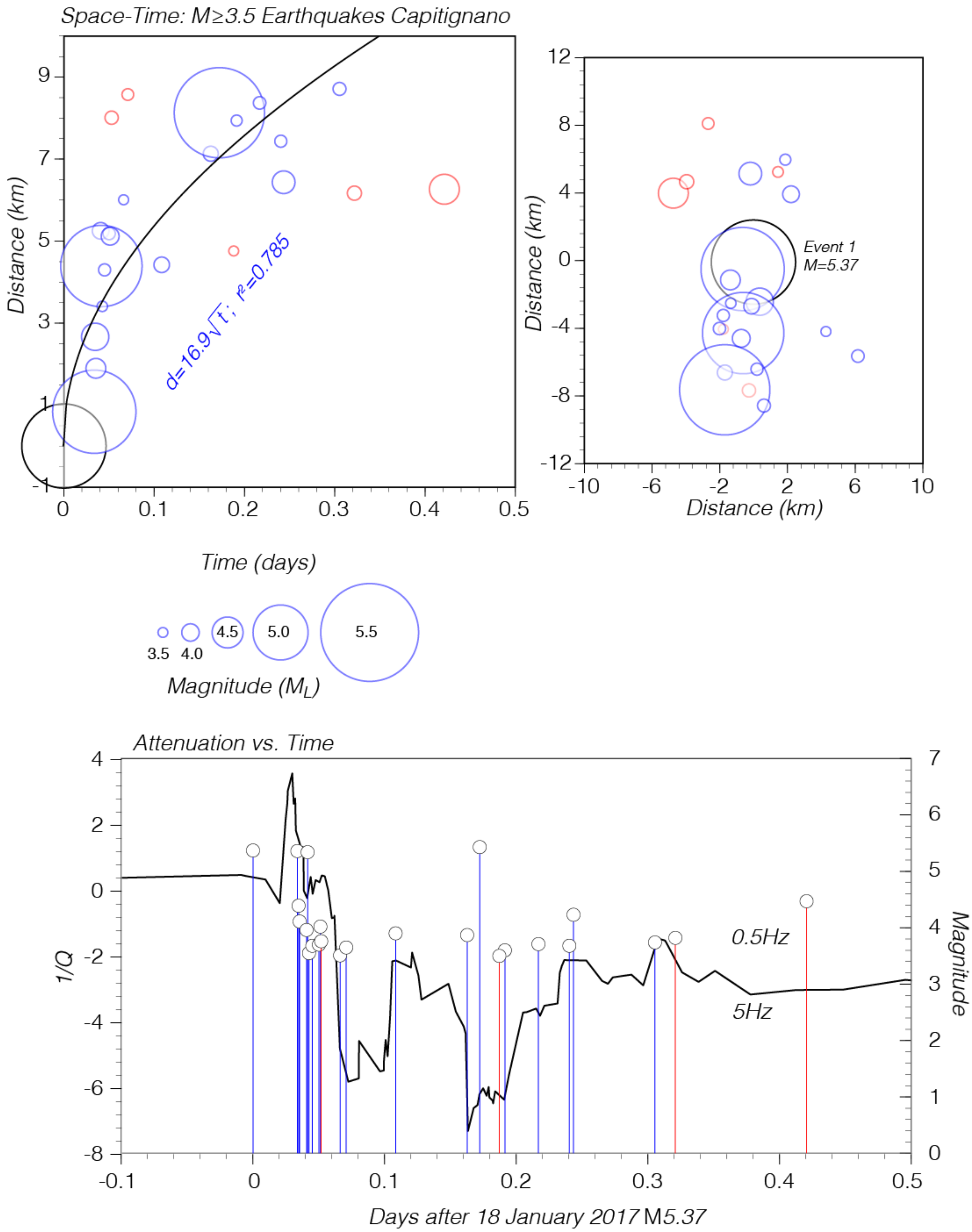

1076

1077 **Figure 8.** **Diffusion and attenuation vs. time: Capitignano. Upper:** diffusion process associated
1078 to the seismic sequence of Capitignano (January 18, 2017). Map view to the right. **Lower:** 2.2 Hz
1079 fluctuation of the seismic attenuation parameter around the pre-Amatrice average. The colors of

the vertical lines associated with earthquakes correspond with the earthquakes portrayed by colored circles in the upper panel.

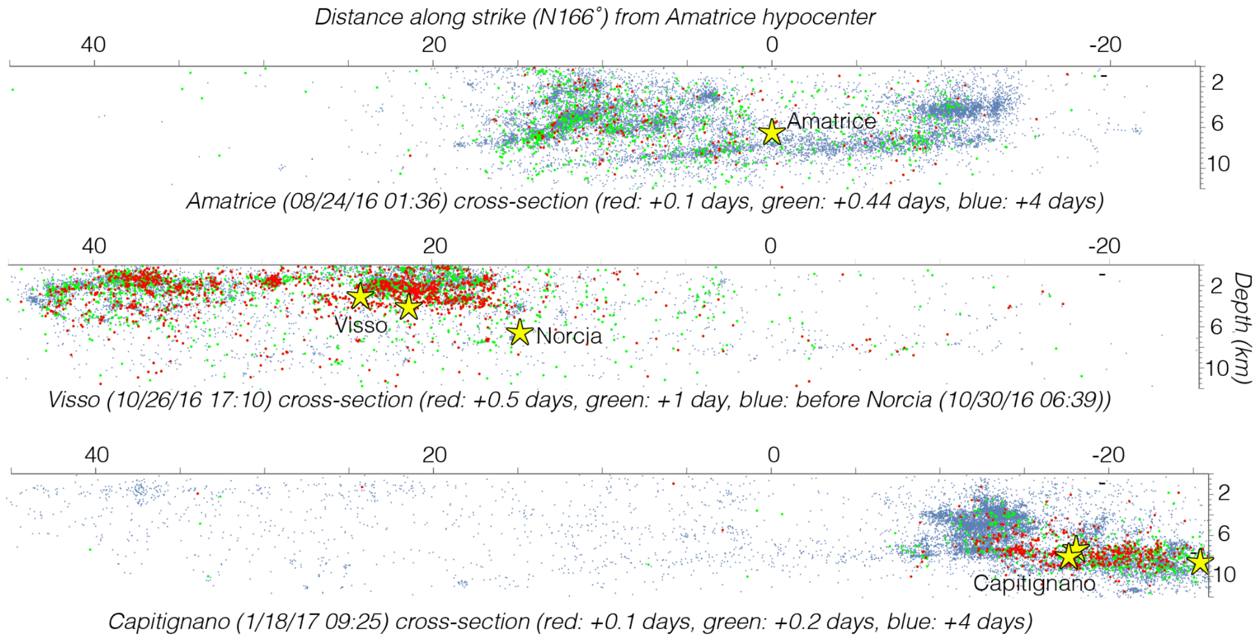

Figure 9. Cross-sectional views of relocated catalogs. Relocated earthquake catalogs of the Central Apennines seismic sequence (Tan et al., 2021). The top panel shows an eastward view that highlights a basal detachment at ~10-15 km depth as well as several structures above it. Red events correspond to the first 0.1 days after the Amatrice mainshock and to the first two diffusion curves in Figure 6, and the green dots include all three diffusion events; these earthquakes highlight potential fluid diffusion pathways along faults. The red events in the center panel correspond in time with the potential diffusion event between the Visso and Norcia shocks (Figure 7). The lower panel shows potential diffusion pathways involving the Capitignano sequence of 4 M≥5 shocks (Figure 8).

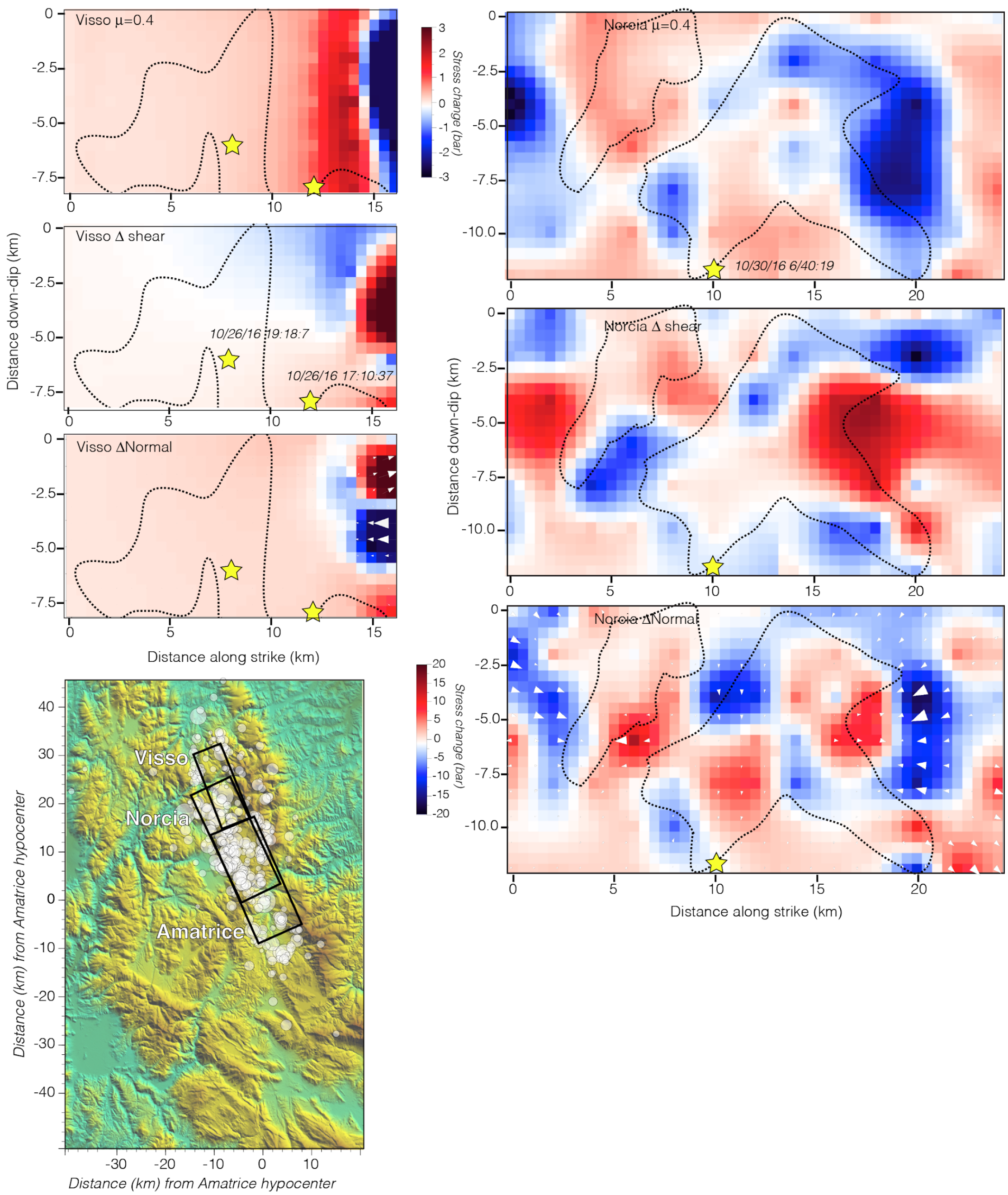

Figure 10. Calculated static stress changes from **M**≥3 earthquakes beginning with the 24 August 2016 Amatrice earthquake resolved on the ruptures of the Visso and Norcia earthquakes (left and right columns, respectively). Hypocenters are shown by yellow stars and approximate slip distributions outlined from solutions by Chiaraluce et al. (2017). Coulomb stress changes are mostly positive on the Visso plane (calculated with an intermediate friction coefficient of 0.4). Shear and normal stress changes are also shown. Expected magnitudes and directions of relative fluid flow resulting from normal stress

changes are superposed on the normal stress change map for both the Visso and Norcia ruptures. The Norcia plane shows very complex patterns of stress change and fluid flow.

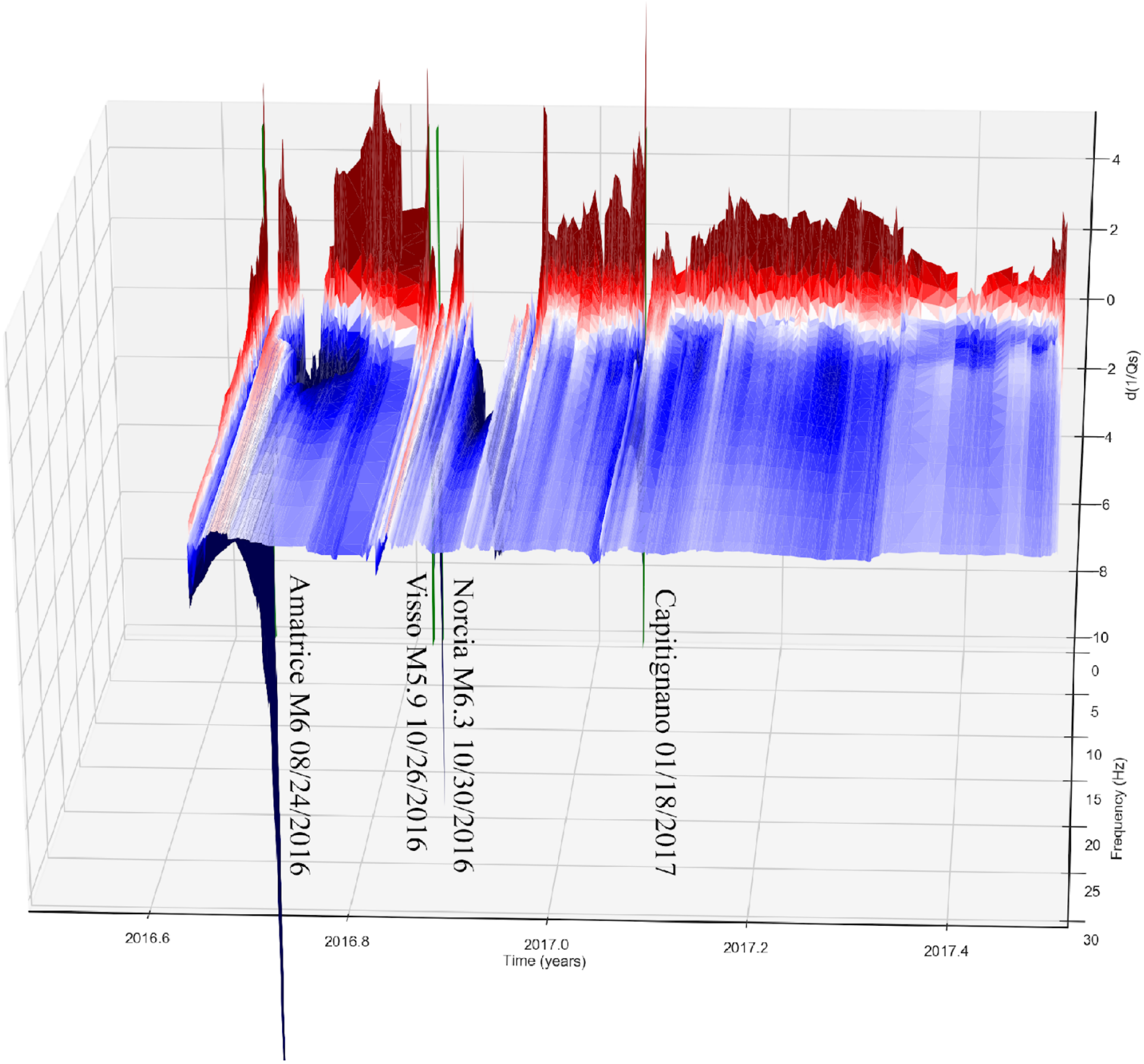

Figure 11. 3D visualization of the seismic attenuation parameter $Q_S^{-1}(f,t)$ during the most energetic part of the Amatrice-Visso-Norcia seismic sequence. Indicated are the occurrences of the three mainshocks and of the Capitignano sub-sequence of January 18 2017. It is very clear that the earthquakes produce a sharp coseismic drop in seismic attenuation at relatively high frequencies (only frequencies $f \geq 1$ Hz are plotted here) due to crack closing (Muir-Wood and King, 1993), followed by a more gentle rise, probably due to fluid displacement through diffusion, and a wide through that is probably due to the cumulative effects of coseismic crack closure produced by the aftershocks. The pattern is reproduced after each main event, and after the Capitignano sub-sequence.

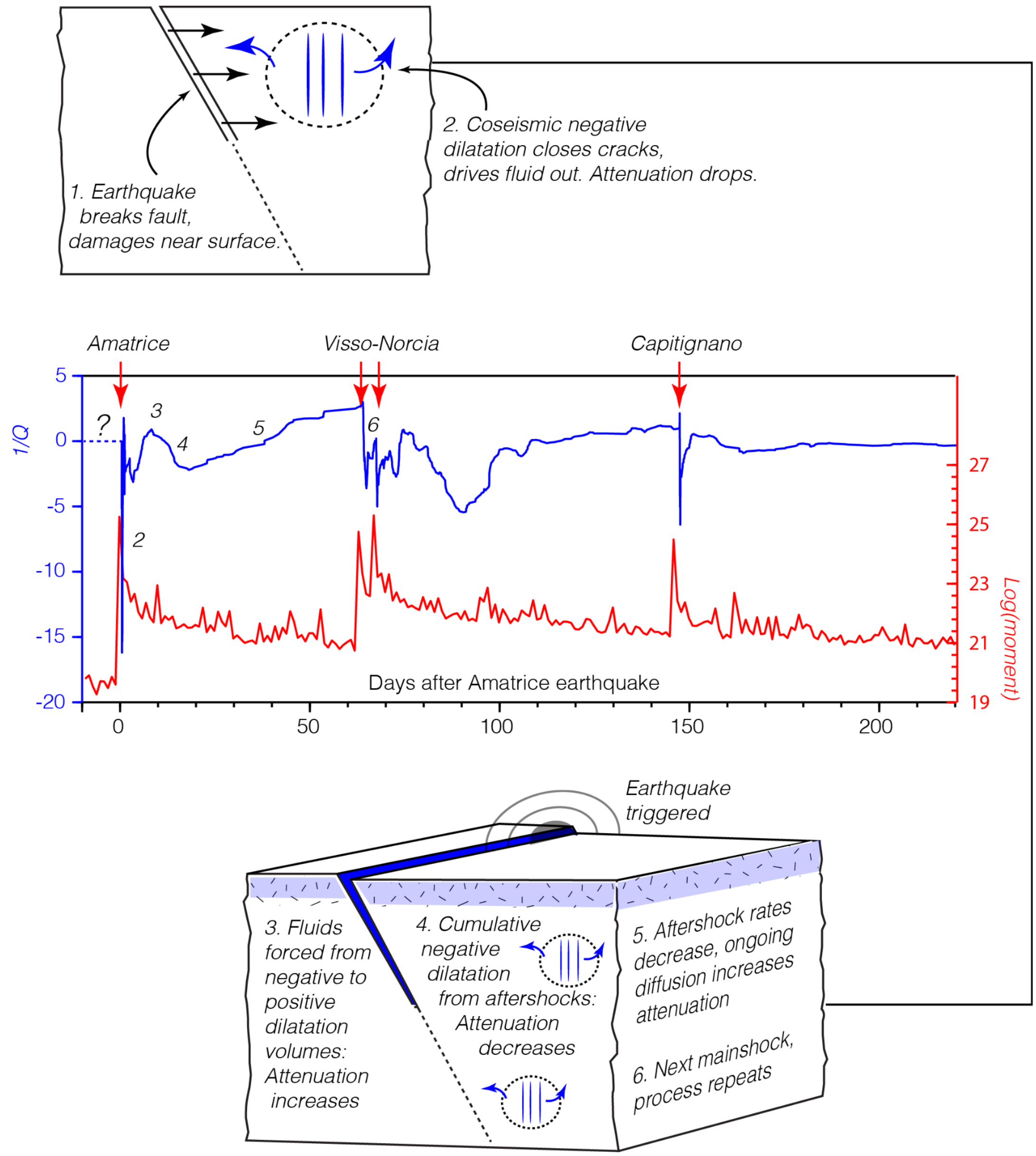

Figure 12. Conceptual model of fluid behavior. Scaling the attenuation vs. time curves from after the Amatrice, Norcia, and Capitignano earthquakes, we note a consistent shape. Each mainshock that initiates a sequence is associated with a sharp increase in $Q_S^{-1}(f,t),\ f = 2.2\ Hz$, followed by a comparatively steep drop. This happens during periods where potential diffusion is also observed. A subsequent gradual recovery in $Q_S^{-1}(\,f,t),\ f = 2.2\ Hz$, persists up until the next mainshock. We hypothesize that this recovery is associated with the redistribution of fluids into newly damaged faults and into the shallow crust. The question mark on the dashed segment of the 1/Q curve indicates that such a horizontal segment is there for a reference purpose only, for we have no information about what happens to the attenuation parameter right before the Amatrice earthquake.